POLITECNICO DI TORINO

Department of Mechanical and Aerospace Engineering (DIMEAS)

Master's degree in Biomedical Engineering

Synthesis and Characterization of Bismuth-based Nanoparticles for Targeted Computed Tomography Imaging

Supervisor

Prof. Valentina Alice Cauda

Candidate

Francesco Mangano

Co-supervisor

Dr. Carly S. Filgueira

Academic Year 2024/2025

Abstract

The cardiac conduction system (CCS) is responsible for rhythmic and coordinated contraction of the heart by rapidly transmitting electrical impulses through fast-conducting fibers. Conduction abnormalities can manifest as life-threatening arrhythmia. Catheter ablation remains the standard treatment for restoring normal cardiac rhythm, relying heavily on accurate localization of the arrhythmogenic substrate. Intraprocedural visualization of CCS abnormalities would be game changing in precisely guiding ablation to the region of interest and minimizing collateral damage of healthy tissue. Although current imaging modalities such as computed tomography (CT) combined with iodinated contrast agents (ICAs) provide high-resolution anatomical detail, they lack the specificity needed to delineate the CCS for targeted intervention. The use of ICAs present several limitations, including nephrotoxicity, short half-life, and risk of hypersensitivity reactions in patients. Bismuth-based nanoparticles (Bi Nps) offer a promising alternative to ICAs due to bismuth's higher atomic number (Z=83) compared to iodine (Z=53), resulting in greater X-ray attenuation. Their nanoscale size enables Bi Nps to evade renal filtration, thereby prolonging circulation time and enhancing the imaging window. Unlike ICAs, Bi Nps can be functionalized with antibodies targeting specific proteins, such as Contactin-2 (Cntn2), which is preferentially expressed on CCS cells. The aim of this work is to synthesize high-payload Bi Nps with strong radiopaque properties that can be conjugated with Cntn2 antibodies, enabling targeted binding to Cntn2-expressing cells.

Bi Nps were synthesized by dissolving bismuth (III) nitrate pentahydrate in 1,2-propanediol, using α-D(+) glucose as a surfactant and borane morpholine as a reducing agent. The synthesized Bi NPs were subsequently PEGylated using a layer-by-layer (LbL) approach, employing poly(allylamine hydrochloride) (PAH) and poly(acrylic acid) (PAA) as polyelectrolytes, followed by the addition of amino-PEG-acid (NH_2-PEG-COOH). PEGylated particles were further conjugated with Cntn2 antibodies using NHS/EDC chemistry.

Dynamic Light Scattering (DLS) and Zeta Potential analyses revealed an average hydrodynamic diameter of 107.8 ± 1.9 nm and a surface charge of -26.6 ± 1.7 mV for

the Bi Nps. Ultraviolet-Visible (UV-vis) spectroscopy showed a broad and stable absorption between 350–400 nm over 20 weeks. Transmission Electron Microscopy (TEM) confirmed the crystalline structure, with a bismuth core-size of 65.6 ± 9.6 nm. MicroCT analysis confirmed significantly higher X-ray attenuation compared to commercial ICAs. The success of the LbL coating was confirmed at each step by DLS analysis, which showed a progressive increase in hydrodynamic diameter. Zeta potential measurements revealed corresponding changes in surface charge, confirming a negative value for the PEGylated particles, which was maintained following Cntn2 conjugation.

In conclusion, Bi Nps demonstrated sustained colloidal stability and superior X-ray attenuation compared to commercial ICAs, reinforcing their potential as a nanoparticle-based alternative for X-ray imaging. Furthermore, Bi Nps were successfully PEGylated and conjugated with Cntn2 antibodies to enable targeted visualization. Their enhanced physicochemical properties and targeting capability highlight their suitability for visualizing the CCS and advancing precision imaging in electrophysiological interventions.

Table of Content

List of Figures

List of Tables

1 Chapter 1 - Introduction

1.1 The Cardiac Conduction System

The Cardiac Conduction System (CCS) is responsible for the initiation and propagation of the cardiac electrical stimuli, responsible for the rhythmic and coordinated contraction of the myocardium, that is required to efficiently pump blood throughout the body.

The impulse originated in the sinoatrial (SA) node, located in the junction between the atrium and the superior vena cava. Here, pacemaker cells spontaneously generate an electrical signal that spreads rapidly through the atrial myocardium, to reach the atrioventricular (AV) node. The electrical stimulus here is delayed, allowing the atria to fully contract and the ventricles to completely get filled with blood. The impulse then enters the His bundle, a group of conductive fibers that crosses the barrier between atria and ventricles, which otherwise would be electrically isolated. From the His bundle, the signal travels rapidly down to the right and left bundle branches and into the Purkinje fiber network, which distributes the impulse throughout the ventricles, triggering a coordinated and efficient ventricular contraction (*Figure* 1). Through this sequential regulated pathway, the CCS ensures a proper synchrony of the cardiac cycle[1,2].

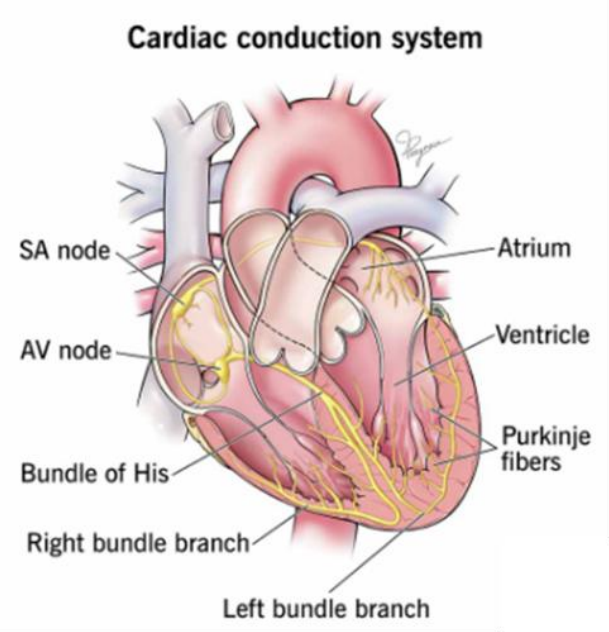

Figure 1: Schematic view of the Cardiac Conduction System. *Picture derived from https://my.clevelandclinic.org/health/body/21648-heart-conduction-system*[3]

When these structures do not work properly, the electrical stimuli can be slowed down, blocked, or misdirect, leading to abnormal heartbeats. These conditions, known as arrythmias, severely affect the hearth's ability to contract in a synchronized and efficient way, because they can reduce the cardiac output and the blood flow to vital organs, becoming life-threatening. For example, hemodynamic compromise can lead to a range of serious clinical consequences such as syncope, cerebral ischemia, hearth failure and, in the most severe cases, cardiac arrest. Additionally, excessively slow rhythms (bradycardia), which consist of ineffective stimulations of the ventricles, may not ensure an adequate oxygen supply to the tissues, while fast rhythms (tachycardia), related to abnormal and uncoordinated electrical impulses, reduce the filling time of ventricles, further decrease the amount of blood pumped out. Thus, the presence of these arrythmias represent an immediate threat to the patient's clinical stability and requires timely and targeted intervention to restore normal heart rhythm and prevent systemic damage.

Currently, the most effective treatment of cardiac arrythmias in patients is the catheter ablation (CA) procedure, that has the goal to eliminate arrhythmogenic tissues. The procedure is carried out, in a minimally invasive way, by inserting one or

more catheters through a peripheral vein (usually the femoral one) and guided to reach the endocardium. Once the targeted area is reached, energy, usually radiofrequency (500–1000 kHz) or cryoenergy, is applied through the catheter directly to the abnormal tissue, in correspondence of the CCS esulting in a thermal controlled lesion (Figure 2). This procedure transforms the arrhythmogenic tissue into a scar tissue that is no longer able to generate or conduct abnormal electrical impulses. The overall effect is the restoration of the normal heartbeat[4].

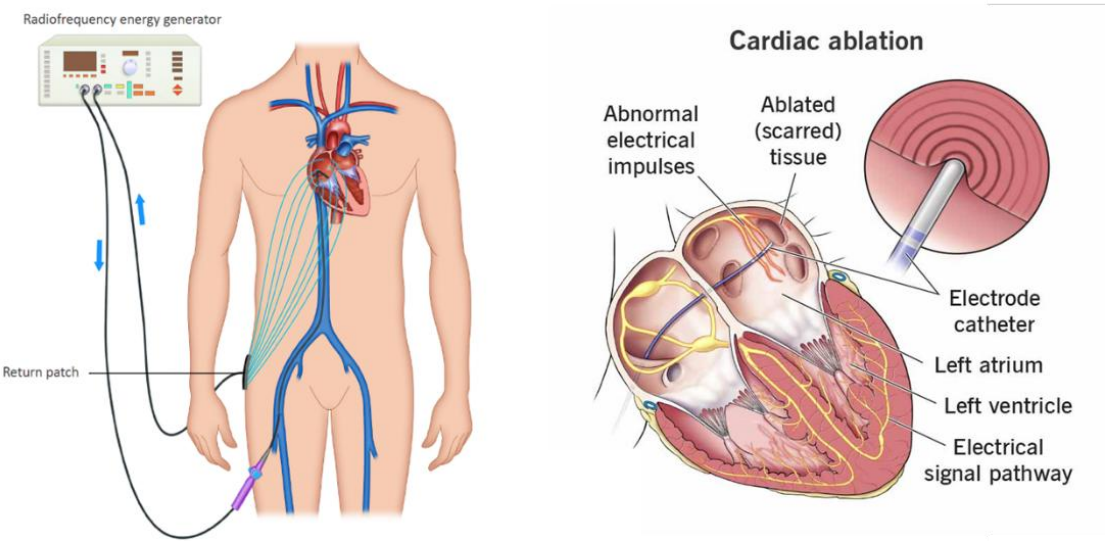

Figure 2: Schematic view of Catheter Ablation procedure. *Picture derived from https://my.clevelandclinic.org/health/treatments/16851-catheter-ablation*[5]

Between 2000 and 2013, the number of catheter ablation procedures performed for the treatment of cardiac arrhythmias in the United States increased significantly. According to data from the National Inpatient Sample (NIS), approximately 520,000 inpatient ablations were carried out during this period[6]). Despite encouraging progress, long-term success rates remain suboptimal, hovering around 60%–70% in patients with persistent atrial fibrillation (AF) and 80%–90% in those with paroxysmal AF[7,8]. These figures, while reflective of important advances, still imply that a substantial proportion of patients, particularly those with persistent AF, may require repeat ablation procedures. Although the introduction of technologies such as 3D electroanatomic mapping, contact force–guided radiofrequency ablation, and

cryoablation has significantly improved safety and efficacy, these approaches remain imperfect. There remains a clear opportunity to refine existing techniques to reduce recurrence and the burden of repeat interventions. Given the non-negligible rates of arrhythmia recurrence and the frequent need for repeat procedures, it is evident that further optimization of catheter ablation strategies is warranted. In this context, advanced imaging modalities have emerged as critical tools to enhance procedural planning and precision. A variety of imaging techniques can be employed to complement and support catheter ablation, offering detailed anatomical visualization of the cardiac chambers and, increasingly, insights into arrhythmogenic substrates. These modalities can help tailor ablation strategies to individual patients, potentially improving long-term outcomes and minimizing the need for repeat interventions. The following chapter will explore these current imaging techniques in greater detail, highlighting their roles in guiding and optimizing catheter ablation procedures.

1.2 Current Imaging Techniques to Support Catheter Ablation Procedure

Multimodal imaging plays an important role since they provide the definition of cardiac chambers anatomy and, potentially even the arrhythmogenic substrates, identifying the area to be ablated and helping to guide the ablation strategies.

Among the most relevant imaging techniques for guiding catheter ablation, Intracardiac echocardiography (ICE) is an imaging technique that involves placing an ultrasound probe on the tip of a catheter, that is further introduced into the cardiac chambers through peripheral veins. ICE provides high-resolution, real-time visualization of cardiac anatomy and catheter position within the heart by using an ultrasound transducer to emit high-frequency sound waves and receive the returning echoes to create dynamic images of intra-cardiac structures with minimal interference such as air or lung artifacts. In catheter ablation procedures, ICE enables precise visualization of cardiac allowing the correct location of the ablating catheter during CA procedure and its contact with tissue[9,10].

Electroanatomic mapping (EAM) is an advanced technology used to create a precise three-dimensional (3D) model of the heart's anatomy combined with electrical[11] activity data. This process involves the use of catheters equipped with sensors that use magnetic fields, impedance or both, to record local electrical signals at multiple points on the endocardial surface[11]. These paired anatomical and electrical data points can be color-coded to create comprehensive heatmaps to visually display the cardiac geometry or arrhythmogenic substrates; for example, low-voltage scar areas or sites of delayed conduction. These maps can be used to guide the ablation catheter navigation to focal sources and slow conduction zones responsible for arrhythmias[9].

Cardiac Magnetic Resonance (CMR) is a non-invasive imaging technology that uses magnetic fields and radiofrequency pulses to produce detailed images of the heart and the great vessels without involving ionizing radiation. It exploits the magnetic properties of hydrogen protons in body tissues; when placed in a strong static magnetic field, these protons align with the field and can be excited by radiofrequency pulses[11]. The emitted signals during relaxation are spatially encoded to create high-resolution images that can be used as pivotal in CA procedure, both pre- and post-procedure, providing detailed anatomical maps of cardiac chambers[9]. Computed tomography (CT) is a medical imaging technique that uses X-rays to produce detailed cross-sectional and 3D images of the body, including the heart and its surrounding structures. These reconstructions help electrophysiologists identify patient-specific anatomical variations and landmarks critical for safe and effective catheter navigation and precise lesion placement during ablation procedures[9,12].

While multiple imaging modalities are employed to support CA, there's still an unmet need, since these technologies can't provide real-time intraprocedural feedback on where to ablate with precision. This represents a critical limitation, because improving outcomes and minimizing recurrence depend on the accurate identification of arrhythmogenic regions during CA procedure itself.

ICE, for example, plays a valuable role in catheter navigation and anatomical visualization, but it does not provide functional feedback to guide ablation targets. Electroanatomic mapping systems can generate heatmaps based on electrical activity and voltage, offering some preliminary insights into ablation effectiveness. However,

they are limited by the inability to visualize the CCS, with the risk of ablating non-target regions. Furthermore, signal interpretation can be ambiguous, especially in structurally abnormal myocardium.

Cardiac MRI provides high-resolution anatomical and structural information but lacks the capability to guide ablation in real time and requires the patient to be moved to a dedicated imaging suite. CT imaging, although capable of offering high spatial resolution and holding promise for integration into procedural workflows, still falls short in distinguishing the CCS from surrounding soft tissue and therefore cannot yet provide dynamic, intraoperative guidance during ablation.

One of the central challenges in CA remains the risk of damaging healthy myocardial tissue due to the absence of precise and anatomical-functional guidance during the procedure. The ability to selectively highlight the CCS and the relevant arrhythmogenic substrates, ideally through advanced intraoperative imaging such as CT, would enable more targeted ablation, reducing collateral damage and enhancing procedural efficacy and safety.

The following section explores the current and future roles of CT imaging in this context, with a particular focus on its limitations and opportunities for optimization as a real-time decision-support tool for guiding catheter ablation procedures.

1.3 Computed Tomography

Computed Tomography (CT), first introduced in 1972 by Godfrey Hounsfield and Allan Cormack, is based on the same physical principles as radiography: using X-rays to obtain internal images of the body. However, in CT the X-ray tube and detector rotate around the patient, capturing images from hundreds of different angles. Each image captures a cross-section (or "slice") of the body. This way, data representing different perspectives of the same anatomical area is collected. The raw data from the two-dimensional images of each slice are sent to a computer, which reconstructs a three-dimensional image. This process allows for the virtual "slicing" of the body into thin

sections, eliminating the overlap of structures typical in traditional radiography. Thus, CT can provide detailed three-dimensional images of internal body structures, enabling them to precisely locate lesions or abnormalities and plan surgical procedures or treatments with greater accuracy. Thanks to this detailed scanning, CT can visualize large-scale structures, such as bones, organs, and tissues in the human body, with spatial resolution ranging from 0.5 mm to 1 mm[13].

1.3.1 X-ray Attenuation Principles

Radiography was first discovered in 1895 by German physicist Wilhelm Conrad Röntgen, X-rays quickly transformed medical practice by providing a non-invasive method to visualize the inside of the human body. X-ray imaging relies on the interaction of X-ray beam with human body tissues. X-rays are a form of electromagnetic radiation with very short wavelengths, typically ranging from 0.01 nm to 0.1 nm[14], allowing them to penetrate solid materials. When an X-ray source emits radiation toward a patient, photons pass through body tissues, interacting differently depending on the density and atomic number of the elements present in those tissues.

A material's ability to attenuate X-rays depends on its attenuation coefficient, which is closely related to the atomic number (Z) of the elements in the tissue and its density. Different tissues, even if composed of similar elements, may appear radiographically distinct if there is a density difference among these elements. Structures like bone tissue, with a high calcium (Z = 20) and phosphate (Z = 15) content, have higher atomic numbers and significantly greater density (density = 1.85 g/cm³) than the other tissues, absorbing more radiation and thus attenuating the X-rays reaching the detector. This creates the typical images seen in radiography, where bones appear lighter, while soft tissues, like muscles (density = 1.06 g/cm³) or fatty tissue (density = 0.91 g/cm^3), appear darker because they absorb less radiation [15].

When an X-ray beam interacts with matter, an X-ray photon is completely absorbed by an atom within the material in a process known as photoelectric absorption. Here, the photon transfers all its energy to an electron bound to the atom, causing the

electron to become excited and expelled from its orbital (becoming a photoelectron), thereby ionizing the atom (Figure 3A). This process is more likely to occur in materials with high atomic numbers (Z), such as bones containing calcium (Z = 20), have a high probability of photoelectric absorption, which means they attenuate X-rays more than soft tissues. Conversely, in soft tissues composed of low atomic number elements, electrons are not tightly bound to the nucleus. When an X-ray photon, strikes a weakly bound or free electron, it transfers much of its energy to the electron and changes direction. This process, known as Compton scattering, does not fully eliminate the photon but reduces its energy and alters its path, while the electron is ejected from the atom (Figure 3B). Compton scattering does not depend significantly on atomic number but rather on the electronic density of the material; it tends to occur in tissues with relatively uniform density, like soft tissues. Compton scattering reduces image contrast, as the deflected photon does not directly contribute to image detail formation[16].

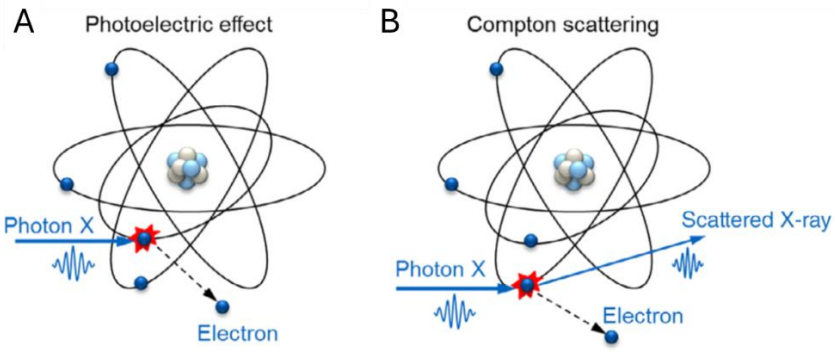

Figure 3: Schematic view of (A) the Photoelectric effect and (B) Compton scattering. *Picture adapted from Hsu et al.[16] showing a*

The overall attenuation of X-rays depends on the combination of photoelectric effect and Compton scattering. It is expressed in terms of the linear attenuation coefficient (μ), which describes how quickly an X-ray beam loses energy as it travels through a material:

$$\mu = \frac{\rho * Z^4}{A * E^3}$$

Where ρ is the density of the material, Z is the atomic number, A is the atomic mass of the elemental constituents, and E is the incident X-ray energy. Notably, the fraction of attenuated radiation depends exponentially on the atomic number of the atoms in the material, since μ is proportional to Z^4. Thus, the calculated μ value is inherently dominated by the Z term.

Therefore, denser materials, which have more atoms per unit volume, and materials composed of elements with a high atomic number, attenuate X-rays to a greater extent; additionally, the higher the energy (E) of the incident X-ray, the lower the attenuation will be.

Since μ is an extensive property, the X-ray attenuation from atoms or materials is additive over a distance. If the atomic composition of a material is known, the material's attenuation can be derived by adding the attenuations from the individual elemental components. In fact, through μ, it is possible to calculate the fraction of emitted radiation that is attenuated by a given material, according to Lambert-Beer's law:

$$\frac{I}{I_0} = e^{[-\frac{\mu}{\rho} * x]}$$

Where I is the transmitted radiation intensity, I_0 is the incident radiation intensity, and μ is the X-ray attenuation, with ρ representing density and x the thickness of the material, which is the linear distance traveled by the X-ray beam through the material[15]. Thus, $1-I/I_0$ represents the fraction of radiation attenuated by a material as its thickness varies, while μ/ρ represents the mass attenuation coefficient of a given element or material as a function of its weight.

The K-edge is another important parameter that defines the energy needed to remove an electron from the innermost shell of an atom, called the K-shell. When the energy of the X-rays used in imaging is just above this threshold, the element's ability to absorb radiation increases sharply, which appears as a peak in attenuation coefficient graphs. This effect is especially important for elements with a high atomic number (Z), such as iodine, barium, gold, lead, and bismuth. Their K-edge values fall within the energy range typically used in medical imaging (33–90 keV), which matches the range of X-ray energies applied in diagnostic radiology. For instance, iodine has a

K-edge at 33.2 keV and barium at 37.4 keV, while gold, lead, and bismuth have higher values (80.7, 88.0, and 90.5 keV, respectively). However, although gold, lead, and bismuth have higher atomic numbers and densities than iodine and barium, this doesn't automatically mean they are always more effective as contrast agents. In the 40–80 keV energy range, iodine and barium often show better performance when considering X-ray absorption per unit of mass. This is because their K-edge lies exactly within this range, leading to a strong increase in attenuation. On the other hand, if we look at attenuation per unit of volume (meaning how much radiation is absorbed in the same physical space), then denser elements like gold, lead, and bismuth can be more effective, simply because there are more atoms packed into the same volume, and therefore more chances to absorb the radiation. From these reasons, the choice of the element to be used as a contrast agent depends not only on its atomic number, but also on the position of its K-edge relative to the imaging energy, the density of the material, and the method of administration. This makes the selection of the contrast agent a highly tailored process, carefully adapted to the specific clinical application.

The ability of matter to attenuate X-rays is quantified in Hounsfield units (HU). Most CT scanners are calibrated using water as a reference, assigning it a "density value" of 0 HU, while air is assigned a value of −1000 HU. For a material with a linear X-ray attenuation coefficient, denoted as "μ," the corresponding HU value is calculated using the formula:

$$HU = \left(\frac{\mu - \mu_{water}}{\mu_{water}}\right) * 1000$$

where μ_{water} is the linear X-ray attenuation coefficient of water. Attenuation values typically range from -1000, 0, and 1000 HU for air, water, and bones, respectively, while the values are within a narrow range between 0 and 100 for soft tissues[14,17].

1.3.2 Clinical Use of CT Applications and Limitations

Computed tomography (CT) plays a central and versatile role across a wide range of clinical applications, since its rapid acquisition time, widespread availability, and integration into diagnostic and interventional workflows have made it indispensable in contemporary healthcare.

In oncology, CT is fundamental for tumor detection, staging, guiding biopsies, and monitoring therapeutic response. Tumors often alter the morphology and density of affected tissues, and CT can detect these changes with high precision. Fro instance, during staging, CT allows clinicians to assess tumor size, involvement of adjacent structures, and the presence of distant metastases. Moreover, it provides real-time guidance during biopsy procedures and enables longitudinal monitoring of treatment efficacy by evaluating morphological changes over time[18]. Its diagnostic performance can be further enhanced when combined with other imaging modalities, such as PET/CT, where metabolic activity detected by PET is precisely mapped onto anatomical structures provided by CT [19]. This combination has proved to be effective in oncology, but also, showed successful applications in, neurology, and cardiovascular disease[19]. In vascular imaging, CT angiography (CTA) provides high-resolution visualization of both arterial and venous structures, facilitating the diagnosis of aneurysms, stenoses, congenital vascular anomalies and planning endovascular or surgical interventions[18]. In trauma and emergency medicine, CT is considered the gold standard for the rapid identification of life-threatening conditions such as intracranial hemorrhages, organ lacerations, fractures, and other internal injuries. These critical findings can directly inform urgent clinical decisions and can significantly improve patient outcomes[18]. In the context of pulmonary imaging, CT enables visualization of fine structures such as distal bronchi and the pulmonary interstitium. This is essential for diagnosing conditions including pulmonary embolism, pneumonia, interstitial lung disease, and COVID-19-related complications. Similarly, in abdominal imaging, CT provides a comprehensive view of intra-abdominal organs, allowing clinicians to evaluate a variety of conditions such as appendicitis, hepatic lesions, renal pathologies, and bowel obstructions[19]. Lastly, CT is also widely applied in the musculoskeletal field, where it aids in detecting bone trabeculae, identifying bone marrow edema, characterizing renal stones, and diagnosing osteomyelitis. It also plays a crucial role in characterizing renal calculi by providing accurate measurements of stone size, density, and location, which are essential for determining appropriate treatment strategies[18].

In each of these domains, CT provides critical anatomical information that directly impacts diagnostic accuracy and patient management. But despite these broad and vital applications, CT does not come without limitations. First of all, its reduced ability to clearly distinguish between tissues with similar attenuation properties: CT is optimal for visualizing dense structures like bones but struggles to differentiate tissues with similar densities, such as soft tissues, blood vessels, muscles, fat, and some tumor formations. This results in images with low contrast and insufficient detail, affecting the accuracy and sensitivity of diagnosis. Another key limitation is radiation exposure. Compared to conventional X-rays, CT delivers a significantly higher dose of ionizing radiation, raising concerns about cumulative exposure, particularly in pediatric patients[20], or individuals undergoing repeat imaging[21]. Moreover, CT may fail to detect very small lesions or microstructural abnormalities due to spatial resolution constraints. This can impact the sensitivity of CT in identifying early or minimal disease, such as metastases or subtle vascular changes[22].

These limitations have driven increased research into contrast agents, to enhance the localization and characterization of such structures, facilitating the identification of tumors, vascular lesions, and other abnormalities that might otherwisenot properly visualized.

1.4 X-ray Medical Contrast Agents

X-ray contrast agents are atoms or molecules formulated with elements of high atomic number (Z), such as iodine (Z = 53) or barium (Z = 56), that can absorb X-rays. Acting as temporary "markers," these molecules that can be injected into the circulatory system to locally enhance X-ray opacity, allowing clearer differentiation in diagnostic images of soft tissues, blood vessels, or small tumors, which would otherwise appear indistinct under traditional X-ray imaging.

So far, the clinical approved contrast agents are iodine contrast agents (ICAs). The X-ray attenuation coefficient of iodine (1.94 cm^2/g) is significantly higher than that of bones (0.186 cm^2/g), and soft tissues (0.169 cm^2/g), making ICAs much more effective at generating contrast in CT imaging[14]. Due to their water solubility, ICAs can be administered via the gastrointestinal tract and intravenously, making them ideal for a variety of applications, including vascular imaging. Soluble molecular contrast agents are primarily filtered by the renal system and eliminated through urine, making them particularly useful for imaging circulatory and renal function. In the United States, the most commonly used ICAs, with Food and Drug Administration (FDA)-approved variants, include iopamidol and iodixanol, which are administered through intravascular injection The ability of an ICA to attenuate X-rays depends on the number of iodine molecules present in the tissue to be imaged and is inversely related to the X-ray energy used for imaging. Therefore, the type and amount of contrast media used for a given purpose also depend on the imaging characteristics required.

1.4.1 Current Limitations of Iodine-based Contrast Agents

Although contrast agents are widely used in clinical practice, their increasing use has also highlighted several limitations that continue to drive research toward improved alternatives.

Acute and chronic reactions to ICAs are influenced by several factors, including the chemical nature of the contrast agent and the volume of the drug administered. For instance, the average daily physiological turnover of iodine is 0.0001 g, while the total iodine content in the human body (mainly in the thyroid gland) is about 0.01 g. An injection of 120 mL of a contrast agent with a concentration of 370 mg of iodine/mL results in 44.4 g of iodine delivered into the body in less than a minute, over 300,000 times the daily turnover of iodine[23].

Acute reactions typically occur within an hour of injection. The severity of these reactions can range from mild, such as injection site pain, nausea, vomiting, rash, or

hemodynamic changes, to very severe, such as respiratory distress, laryngeal edema, hypotension, and cardiovascular collapse[24]. Delayed reactions, which occur at least an hour after exposure and may last up to a week, are usually less severe and primarily manifest as itchy rashes, hives, nausea, and occasionally hypotension.

Another potential complication of using ICAs is contrast-induced nephropathy (CIN), which refers to kidney damage that develops after exposure to the ICA. CIN is diagnosed when there is an increase in serum creatinine concentration greater than 25% within three days of ICA use, provided there are no other obvious causes. Although CIN is rare in patients with normal renal function (with a probability of less than 5%), the high volume of contrast used can be problematic in patients with compromised renal function, reaching up to 50% in patients with severe renal dysfunction. For this reason, the minimum necessary dose is often administered to patients with renal insufficiency[25]. The primary risk factors for CIN include pre-existing kidney disease, advanced age, diabetes, hypertension, and the use of nephrotoxic drugs[26].

Furthermore, ICAs are rapidly filtered by the kidneys, meaning that the half-life of these agents in the body is relatively short (only a few minutes)[27], resulting in a brief imaging window. However, for clear and detailed imaging during diagnostic procedures, the contrast agent must remain in the bloodstream long enough to adequately opacify the targeted tissues. This can be achieved by administering a relatively high dose of contrast or making frequent injections over a short period. As a result, repeated ICAs injections and radiation exposures can occur in some patients with specific imaging requirements, increasing the risk of allergies or other adverse effects.

Additionally, the repeated application of ICAs during diagnostic X-ray procedures, results in a significant increase in radiation-induced DNA damage[28]. This is primarily because the use of these agents requires relatively high X-ray exposure to obtain high-quality images. Prolonged or repeated exposure to ionizing radiation can pose health risks, such as an increased risk of cancers, tissue damage or mutation[29], which is particularly concerning for patients who require frequent scans.

Therefore, there is a clear need to develop alternative strategies for X-ray CT imaging based on the need for a CT contrast agent with minimal dose requirements and improved safety.

1.5 Nanoparticles-based X-ray Contrast Agents

In this context, nanoparticle-based contrast agents have become a focus of research. One of the key requirements of these formulations is their ability to be efficiently eliminated from the body, ideally through renal excretion. This process is regulated by a combination of critical factors, including the particle's hydrodynamic diameter, the surface charge, and to a lesser extent, the shape and density of the core.

The glomerular filtration barrier is highly selective and consists of a fenestrated endothelium (with pores of 70–90 nm), a negatively charged glomerular basement membrane (GBM) with pores of 2–8 nm, and podocytes forming filtration slits of 4–11 nm[30,31]. In this context, it has been established that nanoparticles with a diameter smaller than 5.5 nm can be efficiently cleared by the kidneys through glomerular filtration[27] while the larger ones are quickly taken up by the reticuloendothelial system (RES), especially in the liver and spleen.

This explains why traditional ICAs, which are small water-soluble molecules (<1 nm in diameter) that fall within the size range compatible with renal filtration, exhibit rapid systemic clearance[16]. Therefore, they require high doses to achieve sufficient contrast, that may lead to potential toxicity in patients with impaired kidney function.

On the other side, nanoparticle-based contrast agents, which generally range in size from 1 to 1000 nm, do not easily cross the glomerular filtration barrier and therefore tend to remain longer in circulation. This is a significant clinical advantage for patients with renal impairment, because being large enough to avoid renal clearance leads to longer imaging windows, compared to ICAs, allowing for extended visualization of tissues and organs. This reduces the need for repeated injections and broadens the

clinical use of contrast agents in patients who cannot tolerate iodinated compounds. Their theoretical advantages over traditional ICAs, include also the opportunity to tailor surfactants to minimize adverse biological responses (e.g., functional group display and surface charge), and the potential for site-directed imaging by adding biological targeting groups (such as small ligands, antibodies or peptides) to the particle surface for tissue-specific imaging[32,33]. For instance, as shown in Figure 4 nanoparticles can be functionalized with polymers chains, specific coatings, fluorescent labels and/or targeting ligands. For what concerns the radiopaque component, it can be incorporate into a polymeric nanoparticle, either loaded in the core, embedded in the coating, or bound to the surface, or consist of an inorganic nanoparticle composed of an element with intrinsic X-ray attenuating properties[34].

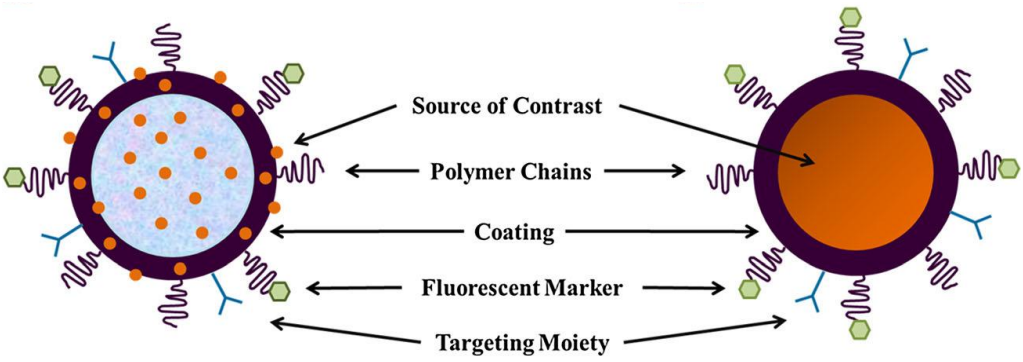

Figure 4: Main strategies to design nanoparticle-based X-ray contrast agents. *Picture adapted from De La Vega & Hafeli[34], representing the The contrast effect can come from either (A) a polymeric nanoparticle where the radiopaque material is loaded into the core, embedded in the coating, or attached to the surface, or (B) an inorganic nanoparticle made of a material that naturally attenuates X-rays.*

Nanoparticles-based X-ray contrast agents can be broadly classified into two categories based on their composition, liposomal iodine-based and metal-based contrast agents.

1.5.1 Liposomal Iodine-based Nanoparticle Contrast Agents

Liposomal ICAs are spherical nanoparticles composed of a double lipid membrane surrounding an aqueous core[14]. Liposomes that incorporate "stealth" properties by including polyethylene glycol (PEG), or other hydrophobic polymers, on their surface and iodine-based cores, such as iohexol or iodixanol, offer numerous advantages over traditional ICAs for vascular and cardiac imaging. Their size, typically around 100 nm, allows for longer circulation times in the bloodstream compared to the traditional non-liposomal ICAs. Additionally, because of their size, stealth liposomes are primarily cleared by RES rather than renal filtration, particularly in the liver and the spleen, where they can persist for long time. Also, due to their prolonged circulation time, liposomes are effective in imaging tumors, leveraging the enhanced permeability and retention (EPR) effect, which enables passive accumulation in solid tumors. However, the iodine concentration in the core of these liposomes may be relatively low, potentially reducing their radiopacity abilities[16].

1.5.2 Metal-based Nanoparticle Contrast Agents

Metal-based nanoparticles, on the other hand, allow for more specific modulation of physicochemical properties, including size, shape, surface charge, and coatings, which directly influence renal excretion and their behavior in the body.

First, metal-based nanoparticles have shown great promise as X-ray contrast agents thanks to their high electron density, which allows for efficient X-ray attenuation, and their ability to carry a much higher payload of contrast atoms compared to traditional ICAs or liposomal-Iodine systems. However, in aqueous or biological environments, these nanoparticles can go through several chemical and physical changes, such as aggregation, adsorption, redox reactions, and dissolution, which consists in the release of metal ions from their surface. The release of metal ions from nanoparticles in biological fluids is an important aspect to evaluate their safety and behavior through body. This process depends on both external conditions and internal features. For instance, the pH of the environment can affect the colloidal stability of

the nanoparticles and influence how easily they release ions into the solution: if they dissolve too quickly their structure can be compromised, and this may reduce their performance as contrast agents. Moreover, the release of metal ions is often linked to toxicity, because these ions can interact with many cellular components like proteins, membranes, and DNA, potentially causing oxidative stress, inflammation, or cell death[35].

At the same time, their surface chemistry plays a key role: nanoparticles with neutral or zwitterionic coatings are cleared more efficiently than those with charged surfaces most likely because they adsorb fewer plasma proteins and have better water solubility[36,37]. Metal-based NPs contrast agents usually have a dense metal core (such as gold, bismuth, tantalum, tungsten, or platinum) and can be coated with materials like polymers, proteins, lipids, or silica to improve their pharmacokinetics, biocompatibility, and stability. In fact, surface coatings can act like a barrier, slowing down the ion release by limiting direct contact with the surrounding environment. For instance, coating them with hydrophilic polymers like polyethylene glycol (PEG) helps prevent aggregation and makes it harder for the immune system to recognize and clear them quickly. PEG chains also increase the overall size of the particles, which means they're less likely to be filtered out by the kidneys. Altogether, the larger size and special surface design help these nanoparticles stay in the bloodstream longer and work more effectively as contrast agents[16].

Among the various metal-based nanoparticles explored for CT imaging, gold (AuNPs) and platinum (Pt-NPs) based contrast agents have emerged as particularly promising due to their high atomic numbers, Z = 79 and Z = 78, respectively, which confer enhanced X-ray attenuation properties compared to traditional ICAs (Z = 53). Pt-NPs, when synthesized using albumin templates, or coated with hydrophilic and biocompatible polymers such as PAA, PAAMA, and PMVEMA, have demonstrated high hemocompatibility and biocompatibility, along with higher contrast efficiency compared to ICAs[38]. AuNPs are among the most studied radiopaque nanomaterials, with a high density (19.3 g/cm^3) and an attenuation coefficient (5.16 cm^2/g at 100 keV) that far exceeds that ICAs, bones (0.186 cm^2/g), and soft tissues (0.169 cm^2/g). This enhanced X-ray attenuation makes AuNPs much more effective than traditional

ICAs at generating contrast in CT imaging, potentially showing a clear delineation of cardiac ventricles and great vessels[39,40]. Moreover, gold exhibits a high biosafety profile, can be synthesized in various sizes and shapes and benefits flexible surface functionalization, offering excellent stability and cellular specificity[14,16].

Although these numerous advantages, he chemical stability of AuNPs, which allows them to remain in the bloodstream for extended periods, may lead to bioaccumulation if administered with repeated uses, potentially causing long-term toxicity issues[40,41]. Furthermore, the high cost of noble metals like gold and platinum poses economic challenges for large-scale production and commercialization[42].

1.6 Bismuth-based Nanoparticles as X-ray Contrast Agent

Although metal-based nanoparticles like gold and platinum have shown great potential as X-ray contrast agents, recent developments in biomedical imaging have highlighted some important limitations.

The selection of elemental bismuth (Bi) as an inorganic nanoparticle core for the functional atoms in nanoparticle-based contrast agents has gained attention for CT imaging. Bismuth is a heavy metal, but unlike its neighbors in the periodic table (such as lead and mercury), it has a relatively low intrinsic toxicity[43]. It is commonly used in over-counter medications, such as bismuth salicylate, which is used to treat gastrointestinal disorders by forming a protective layer on the stomach lining[44].

Bismuth has unique chemical and physical properties, enabling superior X-ray absorption with high biocompatibility. In fact, bismuth has a higher atomic number (Z = 83) compared to gold (Z = 79) and iodine (Z = 53), and a K-edge absorption that surpasses other non-radioactive elements (Bi: 91 keV; Au: 81 keV; I: 33 keV). These characteristics provide excellent X-ray attenuation, even at lower doses[16]. Additionally, bismuth is moderately abundant and cost-effective than gold or platinum. These properties make bismuth the heaviest Z element suitable for use as

an CT contrast agent. Its potential biological compatibility further enhances its suitability for this application.

In recent years, preclinical research has significantly advanced our understanding of bismuth-based nanoparticles (Bi Nps) as next-generation agents for diagnostic imaging and therapeutic interventions. A growing body of evidence supports the multifunctionality of Bi Nps, showcasing their potential as biocompatible, targeted, and theranostic platforms. Their unique physicochemical properties, high atomic number, tunable surface chemistry, and low toxicity profile have made them the subject of extensive *in vitro* and *in vivo* investigations.

In the following sections, we will present and critically analyze the major preclinical studies that have investigated the biocompatibility, multimodal imaging capabilities, theragnostic applications, and active targeting strategies of Bi Nps. Together, these studies form the foundation for their potential clinical translation and integration into advanced diagnostic and therapeutic regimes.

1.7 Preclinical Evaluation of Bismuth-based Nanoparticles

1.7.1 Biocompatibility and Cytotoxicity Profile

The biocompatibility of bismuth nanoparticles (Bi Nps), defined as their ability to interact with biological systems without causing adverse effects, is closely related to the nature of their surface coating, which regulates colloidal stability, systemic circulation, biodistribution, and cytotoxicity.

1.7.1.1 *In vitro* toxicity:

In a reported study[45], bismuth nanoparticles (Bi Nps), synthesized using polyvinylpyrrolidone (PVP) as a colloidal stabilizer, were found to be quickly

recognized and taken up by the immune system, and showed a stronger cytotoxic effect against HeLa cells within 4 days. To reduce these effects, the particles were functionalized with either a porous silica coating (Bi@SiO_2) or PEG (Bi Nps@PEG), resulting in a progressive reduction in cytotoxicity by 20% and 24%, respectively, compared to uncoated Bi Nps. In the case of silica coating, the lower toxicity was likely due to a reduced release of Bi^{3+} ions, which helped to lower the oxidative stress on cells. For PEG-coated particles, the reduced surface charge decreased interactions with the cell membrane, limiting the binding to cellular receptors and reducing adhesion. Another strategy to improve colloidal stability and prevent aggregation involves the use of sugar-based coatings. Sugars such as glucose, lactose, and sucrose can act as capping agents, forming a protective layer on the nanoparticle surface that maintains stability in aqueous environments. Among these, glucose showed the best performance, offering moderate stability, reduced aggregation, and consistent particle size even after irradiation[46]. In this study, glucose-coated Bi Nps showed low cytotoxicity on HeLa cells after 24 hours of incubation at concentrations up to 0.5 mg/mL. Building upon this initial formulation, two independent studies explored further surface modifications to enhance biocompatibility. In one case, glucose-coated Bi Nps were functionalized with methoxy-PEG (mPEG-Bi Nps)[47], while in the other with mesoporous silica combined with PEG (Bi@mSiO_2-PEG)[48]. The enhanced biocompatibility brought by these surface modifications, improved cellular tolerance as well, maintaining cell viability above 90% in both HeLa and HUVEC cells after 24–48 hours of exposure, at concentrations up to 0.3 mg/mL and 0.2 mg/mL, respectively, for both coatings.

1.7.1.2 *In vivo toxicity:*

Although it has been shown that elemental Bi Nps can undergo oxidation and gradual degradation, releasing Bi^{3+} ions that are later eliminated through the kidneys[46], these transformation processes make it difficult to predict their behavior in vivo. Therefore, specific safety studies have been conducted to evaluate their use in preclinical applications.

Wei *et al.*[49] synthesized Bi Nps coated with oligosaccharides and administered them orally to Kunming mice to study their application in gastrointestinal tract imaging by CT. At a dose of 280 mg/kg, the main liver and kidney function markers, such as ALT, AST, BUN, creatinine and urea, did not show any significant changes compared to control animals. This dose is comparable to 4.2 g of bismuth salicylate, which is normally administered to treat stomach diseases, suggesting that Bi Nps are safe for oral administration[50]. For what concerns intravenous injection (IV), Swy *et al.*[51] studied bismuth nanoparticles encapsulated in PLGA and administered them to Sprague-Dawley (SD) rats. At a dose of 20 mg/kg, they observed a temporary increase in ALT, AST liver enzymes after 24 hours, along with mild liver and kidney injuries, such as periportal inflammation and damage to renal tubules. Chen *et al*.[52] synthesized and administered Bi_2S_3 nanoparticles coated with Pluronic F127, at very high doses (600 mg Bi/kg) to Balb/C mouse models, showing only a temporary increase in ALT and AST. In all these cases, the altered liver markers returned to normal within a few days, indicating that the observed effects were transient and reversible.

These *in vivo* and *in vitro* studies show that both the biocompatibility and colloidal stability of Bi Nps can vary greatly depending on the type of surface coating used. Therefore, choosing the right one[17] is a key factor to ensure the effectiveness and safety of these nanoparticles in clinical applications.

1.7.2 Multimodal Imaging Capabilities

Bi Nps are not only excellent contrast agents for CT imaging due to their strong X-ray attenuation and their biocompatibility especially when further coated, but they also hold great promise for multimodal imaging. They can be engineered to exhibit photothermal, photodynamic, photoacoustic and even radiotherapeutic properties. By combining these capabilities with CT, it becomes possible to achieve more accurate imaging, providing both anatomical and functional information.

In a study conducted by Bi *et al.*[53] small Bi Nps with a diameter of approximately 4 nm were made water-soluble by PEG coating and subsequently injected intravenously into mice. The nanoparticles showed prolonged circulation times, attributed to the PEG layer, and a preferential accumulation in the liver and intestines; due to their high atomic number, exhibited remarkable X-ray attenuation efficiency. On the other hand, the same Bi Nps were also evaluated for fluorescence imaging, a technique that relies on the light emission of fluorescent molecules or materials to non-invasively visualize tissues or cells. In this case, an in vivo fluorescent signal was detected after excitation at 600 nm, initially localized in the chest and epigastric regions, and later in the hypogastric area. This distribution was consistent with CT imaging results, confirming the potential of Bi Nps for dual-modality applications.

Bi Nps have also been explored for photoacoustic imaging (PAI), which is based on the photoacoustic effect, where light absorbed by tissues or nanoparticles generates an acoustic wave that is then detected by an ultrasound transducer. In these studies Bi Nps were coated with metoxy-PEG[47] or labeled with peptides[54], demonstrating that Bi Nps can also generate a surface plasmon resonance (SPR) effect, in which free electrons on the surface of the particles oscillate in response to an electromagnetic field, resulting in strong optical absorption. Compared to conventional ultrasound, which relies on the mechanical properties of tissues, PAI provides contrast based on optical absorbance, improving the ability to distinguish between different types of tissues.

1.7.3 Theragnostic Applications

Additionally, Bi Nps have been extensively studied for theragnostic applications, combining advanced imaging techniques with therapeutic interventions in a single system. One of the most promising strategies is the integration of imaging with photothermal therapy (PTT) based on near-infrared (NIR) irradiation. This technique uses photothermal agents that, after absorbing NIR light, generate enough heat to

irreversibly damage tumor tissues. Therefore, its therapeutic efficacy strongly depends on the ability of the photothermal agent to convert light energy into heat.

Bi Nps coated with polyvinylpyrrolidone (PVP) have shown excellent properties for both computed tomography (CT) and photothermal imaging-guided PTT [55]. The combination of CT imaging, PTT, and radiotherapy (RT) has also been tested to enhance treatment efficacy. These nanoparticles exhibited high photothermal conversion efficiency and good photostability. In vivo, in a mouse model with UT4 tumors, intravenous injection of Bi@PVP NPs followed by irradiation with an 808 nm laser (1.3 W/cm²) led to a significant temperature increase at the tumor site and resulted in complete inhibition of tumor growth within 14 days.

Another example involves lipophilic Bi Nps coated with dodecanethiol and encapsulated in PEGylated phospholipids (Bi@SR-PEG), which proved effective for both CT imaging and combined PTT and radiotherapy (RT) treatment [56]. These nanoparticles showed a strong photothermal effect under NIR irradiation (808 nm, 1 W/cm²) and a strong radiosensitizing effect after exposure to X-ray irradiation, significantly reducing the number of 4T1 tumor cells *in vitro* and inhibiting tumor growth on *in vivo* mouse models. These results highlight their dual function as radiosensitizers and photothermal agents.

In conclusion, the integration of multiple imaging and therapeutic modalities within a single bismuth-based nanoparticle platform represents a powerful advancement in the field of nanomedicine. Bi Nps have proven to be not only excellent contrast agents for CT, but also effective in enhancing photoacoustic or infrared thermal signals. At the same time, their strong photothermal properties, along with their ability to serve as radiosensitizers, enable synergistic cancer therapies, such as PTT, RT or chemodynamic treatments. This multifunctionality allows for precise diagnosis, guided therapy, and real-time treatment monitoring, making Bi Nps promising candidates for future theranostic application.

1.7.4 Strategies for Active Targeting

Bi Nps have shown great promise for targeted imaging, particularly when combined with strategies that enhance their accumulation at specific tissues or sites. One of the most effective strategies is active targeting based on ligand–receptor interactions, where Bi Nps are functionalized with molecules (including peptides, antibodies, or polymers that recognize and bind specific receptors on cells or tissues.

For example, *Pan et al.*[57] showed that bismuth nanoparticles coated with phospholipids and anti-fibrin monoclonal antibodies were able to selectively bind to unstable atherosclerotic plaques, which are rich in fibrin compared to normal arterial walls. In addition, Li *et al*.[48], developed core-shell bismuth sulfide nanoparticles encapsulated in mesoporous silica and conjugated with trastuzumab, an antibody targeting the HER2 receptor. This system demonstrated strong targeting ability toward HER2-positive human breast cancer cells, showing effective performance in both image-guided diagnostics and therapy. In another study Bi_2Se_3 nanoparticles were modified with anti-CD47 antibodies. CD47 is a protein commonly overexpressed on the surface of tumor cells, that binds to SIRPα receptors on macrophages and inhibiting their phagocytic function against tumor cells. By blocking this CD47–SIRPα interaction using anti-CD47 antibodies conjugated to the nanoparticles, Bi_2Se_3 enhanced the macrophages' ability to recognize and engulf tumor cells. This not only promoted a stronger immune response but also improved the effectiveness of photothermal therapy, as the Bi_2Se_3 were more efficiently retained and activated within the tumor environment[17].

These findings confirm that antibodies, due to their high affinity and specificity for antigens selectively expressed in diseased tissues, can be effectively used to provide Bi Nps with targeted recognition capabilities[17]. The combination of the strong X-ray attenuation of bismuth and the specificity of antibody-based targeting enables not only precise localization of biological targets through CT or multimodal imaging, but also the delivery of therapeutic effects directly to the site of interest.

1.8 Contactin-2 as a Potential Target for CCS Imaging

Despite the broad spectrum of studies demonstrating the potential of Bi Nps in biomedical applications, including multimodal imaging, image-guided therapy, and active targeting through antibody conjugation, there is still a significant gap in literature. So far, no reported Bi Nps formulations have demonstrated the ability to selectively visualize the cardiac conduction system (CCS) using CT. This represents a significant unmet need in cardiovascular imaging and intervention, as high-resolution and specific visualization of the CCS could provide substantial clinical benefits. Such capabilities would enable non-invasive identification of CCS abnormalities and offer critical guidance during CA procedures by facilitating real-time localization of arrhythmogenic tissue for the treatment of cardiac arrhythmias.

An important advance in the molecular understanding of the CCS is represented by the identification of Contactin-2 (Cntn2) as a novel specific marker. Cntn2 is a cell adhesion molecule belonging to the immunoglobulin superfamily, previously known for its role in the central nervous system, where it contributes to axonal guidance, fasciculation, and ion channel clustering. In the heart, Cntn2 expression is significantly enriched in Purkinje fibers compared to working myocardium, but it also involves the sinoatrial node, atrioventricular node, and His bundle, indicating widespread expression throughout the entire CCS, as demonstrated by comparative transcriptomic analysis in CCS-lacZ transgenic mouse hearts[58].

This means that a specific antibody, can be used to target cells expressing Cntn2, which is anchored to cell membranes by a GPI (glycosylphosphatidylinositol) linkage. This topological arrangement makes its Cntn2 epitopes, that are the specific regions recognizable by the antibody, readily accessible, thus promoting antibody–antigen interaction and enabling effective identification of Cntn2-expressing cells.

1.9 Aim of the Work

The aim of this thesis is to synthesize Bi Nps with enhanced X-ray attenuation properties compared to traditional ICAs, for potential applications in targeted CT imaging of CCS. To achieve this, two bottom-upsynthesis methods will be explored using the same chemical precursors. In both protocols, bismuth (III) nitrate pentahydrate is used as the bismuth-salt precursor, morpholine borane as the reducing agent, and α-D(+)-glucose as a stabilizing and capping agent. The reaction will be carried out in 1,2-propanediol (PPD) as common solvent yielding high-payload glucose-coated Bi Nps. The glucose coating formed during synthesis is expected to contribute to the colloidal stability of the Bi Nps in aqueous environments, further improving their biocompatibility. The synthesized nanoparticles that demonstrate the best performance in terms of stability, morphology, and chemical properties, between the two methods, will be selected for further functionalization steps. The functionalization process will be addressed through a layer-by-layer (LbL) electrostatic coating approach, involving sequential deposition of poly(allylamine hydrochloride) (PAH), a cationic polyelectrolyte rich in primary amines, and poly(acrylic acid) (PAA), an anionic polyelectrolyte bearing carboxyl groups. A final coating layer will be applied using a heterobifunctional polyethylene glycol (PEG) molecule, specifically amino-PEG-acid (NH_2-PEG-COOH). The amino terminus (-NH_2) was used to anchor the PEG to the nanoparticle surface by crosslinking the three layers through EDC chemistry, while the terminal carboxyl group (-COOH) will provide a reactive handle for subsequent conjugation.

Overall, this thesis provides an optimized and scalable protocol for the synthesis and PEG-based functionalization of bismuth nanoparticles, yielding stable and biocompatible colloidal formulations suitable for further antibody conjugation with (Cntn2) specific antibody. These functionalized nanoparticles are designed to be used as targeted CT contrast agents for specific visualization of the CCS. The following sections describe and discuss the synthesis strategies, optimization parameters, surface functionalization steps, and the physicochemical and biological characterization techniques employed, along with the corresponding results.

2 Chapter 2 - Materials & Methods

This section outlines the experimental procedures used to synthesize glucose-coated bismuth nanoparticles (Bi Nps) and their surface functionalization with polyethylene glycol (PEG) using a layer-by-layer (LbL) approach. It also describes the main techniques used to characterize the nanoparticles, including analyses of their size, surface charge, colloidal stability, chemical composition, and X-ray attenuation properties.

Bi Nps were synthesized by dissolving bismuth (III) nitrate pentahydrate (Mw = 485.07 g/mol, 98%,) in 1,2-propanediol (Mw = 76.10 g/mol, 99.5% min) using α-D(+) glucose anhydrous (Mw = 180.16 g/mol, 99%+) as a surfactant and borane morpholine complex (Mw = 100.96 g/mol, 97%, Alfa Aesar, Haverhill MA), as a reducing agent. All these compounds have been purchased from Thermo Scientific Chemicals. For the nanoparticle functionalization through a Layer-by-layer approach, poly(allylamine hydrochloride) (PAH) (Mw = 17.500 g/mol) and poly(acrylic acid) (PAA) (Mw = 2000 g/mol, 50 wt. % in H_2O, electronic grade) were employed as polyelectrolytes, Amino-PEG-Acid (NH_2-PEG-COOH) was used as the heterobifunctional polyethylene glycol (PEG) (M_N = 5000 g/mol). All these compounds have been purchased from Sigma Aldrich. The coupling between layers was facilitated using 1-ethyl-3-(3-dimethylaminopropyl) carbodiimide hydrochloride (EDC) (Mw = 191.70, ≥ 98%) as the crosslinking agent, that was purchased from Thermo Scientific Chemicals. Milli-Q water has been obtained by a Millipore water purification system (Millipore). All other reagents were of analytical grade.

2.1 Preparation of Bismuth Nanoparticles

In this thesis work, bismuth-based nanoparticles were synthesized by modifying an already established protocol from Brown *et al*[46], which was then compared in terms of resulting particles with a second method described by Li *et al*[48]. Both methods are

based on a bottom-up synthesis approach, that involves the reduction of Bismuth(III) Nitrate Pentahydrate salt which supplies electrons to produce bismuth (0) nanoparticles and Borane morpholine used as reducing agent. α-D(+)-Glucose will act as a biocompatible organic surfactant, serving as a capping agent to stabilize the nanoparticles. 1,2-Propanediol will be used as the common solvent for all the compounds throughout the reaction stages.

The differences and advantages of the methods are further discussed in Chapter 3

2.1.1 Synthesis of Bismuth Nanoparticles: Brown's Protocol

According to the Brown's method, bismuth nanoparticles were synthesized starting from a 250 mM solution of Bismuth Nitrate Pentahydrate ($Bi(NO_3)_3 \cdot 5H_2O$), dissolved in a saturated 3.56 M solution of α-D(+)-Glucose anhydrous ($C_6H_{12}O_6$). The solution was then heated to 80°C, the reaction temperature at which a 250 mM solution of Morpholine Borane ($C_4H_{12}BNO$) was added, initiating the reduction of bismuth (III) to bismuth (0). All the solutions were prepared by dissolving the reagents in the common solvent 1,2-Propanediol ($C_3H_8O_2$) (PPD).

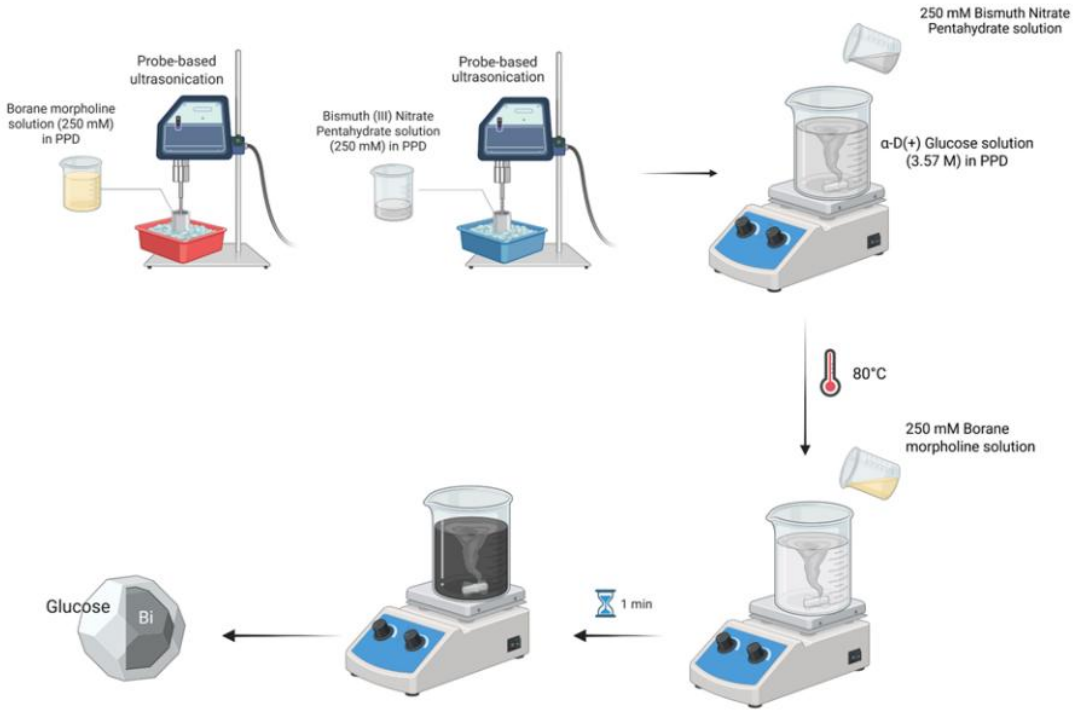

Figure 5: Picture of Bi Nps synthesis according to Brown's protocol

Firstly, 54 g of α-D(+)-Glucose, 0.450 g of Bismuth(III) Nitrate Pentahydrate and 0.308 g of Borane morpholine complex were accurately weighed using a digital precision balance.

Bismuth (III) Nitrate Pentahydrate was completely dissolved in 4 mL of PPD, with stirring at 1,500 rpm for 45 minutes. Glucose powder was added to a 500 mL three-neck round-bottom flask containing 84 mL of PPD and stirred at 1,200 rpm. The flask was placed in a silicone oil bath (usable range from - 40 °C to + 200 °C, ThermoFisher Scientific) for controlled heating, and a thermometer was inserted to monitor the solution temperature in real time. Meanwhile, Morpholine Borane was dissolved in 12.2 mL of PPD and stirred at 1,500 rpm for 20 minutes.

To investigate the influence of glucose dissolution on nanoparticle synthesis, the reduction step was carried out under two different conditions: in the first, glucose was fully dissolved under vigorous stirring (1200 rpm), and once the solution turned clear and reached 80 °C, the bismuth precursor solution was added, followed by the reduction reaction. In the second condition, the bismuth precursor was added to the glucose solution at room temperature, while the glucose was still partially dissolved under the previous stirring conditions. In both cases, once the solutions reached 80 °C, the morpholine borane solution was rapidly added all at once to the reaction mixture: the solution gradually changed color from white to black, indicating the reduction of bismuth (III) ions to metallic bismuth (0), resulting in nanoparticles formation. After 60s from the beginning of the reduction step, the solution was quenched in a 200 mL ice-cold Milli-Q water bath (~ 4°C) and allowed to cool to room temperature for 5-10 minutes.

Nanoparticles purification:

The colloidal solution is then purified to separate the obtained particles from the supernatant, which contains excess reagents (e.g., PPD and glucose) and reaction byproducts (e.g., borate).

More specifically, after quenching the reaction, the colloidal solution was split in sixteen 50mL Centrifugal Tubes, by diluting 20 mL of Bi Nps suspension with 30 mL of MilliQ water and then centrifuged at 3,000 rcf (~4,300 rpm) for 60 minutes. During this time, the larger and denser nanoparticles tend to sediment at the bottom of the tube, forming a pellet, while the smaller and less dense particles remain in suspension in the supernatant.

The supernatant is carefully removed, ensuring the pellet remains intact at the bottom. At this stage, the pellet in each tube is resuspended in 0.5 mL of MilliQ water, combined all together and sonicated for 10 minutes to fully and homogeneously disperse the Bi Nps in suspension.

To further purify the synthesized particles, two different dialysis setups were tested. Initially, 10 mL dialysis membranes (MWCO 8-10 kDa, Spectrum™ Spectra/Por™ Float-A-Lyzer™ G2 Dialysis Devices), filled with Bi Nps suspension, were immersed in a large dialysate bath containing 5 L of MilliQ water. To assess whether the dialysis process influenced particle stability, a second setup was tested and compared to the initial one: multiple 1 mL Float-a-Lyzer membranes were used instead, all immersed together in a reduced volume of 1.5 L of MilliQ water. In both cases particles were kept under gentle magnetic stirring (80 rpm) for 16 hours at room temperature. The concentration difference between the dialysate and the membrane interior creates a concentration gradient. Since the dialysis membrane is semipermeable, through a diffusion process, it allows smaller molecules such as glucose residues or excess chemicals to pass through the membrane and disperse into the dialysate, while larger molecules like the nanoparticles remain inside the membrane.

Nanoparticles filtration:

The final step of this protocol involves filtering the purified aqueous Bi Nps through a filter with specific pore sizes, separating the particles based on their size. The larger particles are retained by the filter, while the smaller ones pass through. This ensures that the particles subjected to filtration have very similar sizes or at least do not exceed the pore size of the filter.

Therefore, after 16 hours of dialysis, the particles are collected and transferred to a Centrifugal tube. There, they are resuspended and sonicated in a water bath for 15 minutes at room temperature. The particles are then filtered by passing the suspension through a 0.45 µm filter (Cytiva Whatman™ Puradisc 25mm Syringe Filters: Sterile, Fisher Scientific).

First, each filter is initialized and hydrated by injecting pure MilliQ water through a 5 mL microsyringe. Then, the syringe is filled with 2 mL at a time of Bi Nps suspension and passed through the filter into another tube. To avoid excessive loss of nanoparticles due to repeated use of the same filter, where particles may become trapped in its pores, the filter is replaced after filtering 4 mL of suspension. Finally, the filtered aqueous BiNps are stored at 4°C for future characterizations.Two modifications were then made to this protocol to evaluate their effect on the final yield. These variants were directly compared to the original protocol (Original). The first modification (Variant 1) involved doubling only the amount of reducing agent: thus, the concentration of Morpholine Borane was increased from 250 mM to 500 mM by dissolving 0.616 g of the compound in 12.2 mL of PPD, while all other reagents were kept at their original quantities.

In the second modification (Variant 2), instead of increasing just the borane concentration, the amount of each reagent was doubled while maintaining the same concentrations. Specifically, 0.970 g of Bismuth nitrate pentahydrate and 0.616 g of Morpholine Borane were weighed and dissolved in 8 mL and 24.4 mL of PPD, respectively, both corresponding to 250 mM solutions. The glucose amount, however, was kept constant at 54 g, but dissolved in double amount of PDD, from 84mL to 168mL, reducing its concentration from 3.57 M to 1.78 M.

2.1.2 Synthesis of Bismuth Nanoparticles: Li's Protocol

As previously introduced, an alternative procedure of nanoparticles preparation was also investigated to understand which one of the two protocol provides better particles formulation and yield. The alternative protocol, carried out with some modifications, uses the same precursors and chemistry, but it differs from the quantity of glucose surfactant used while the relative concentrations of reducing agent and salt precursor are the same.

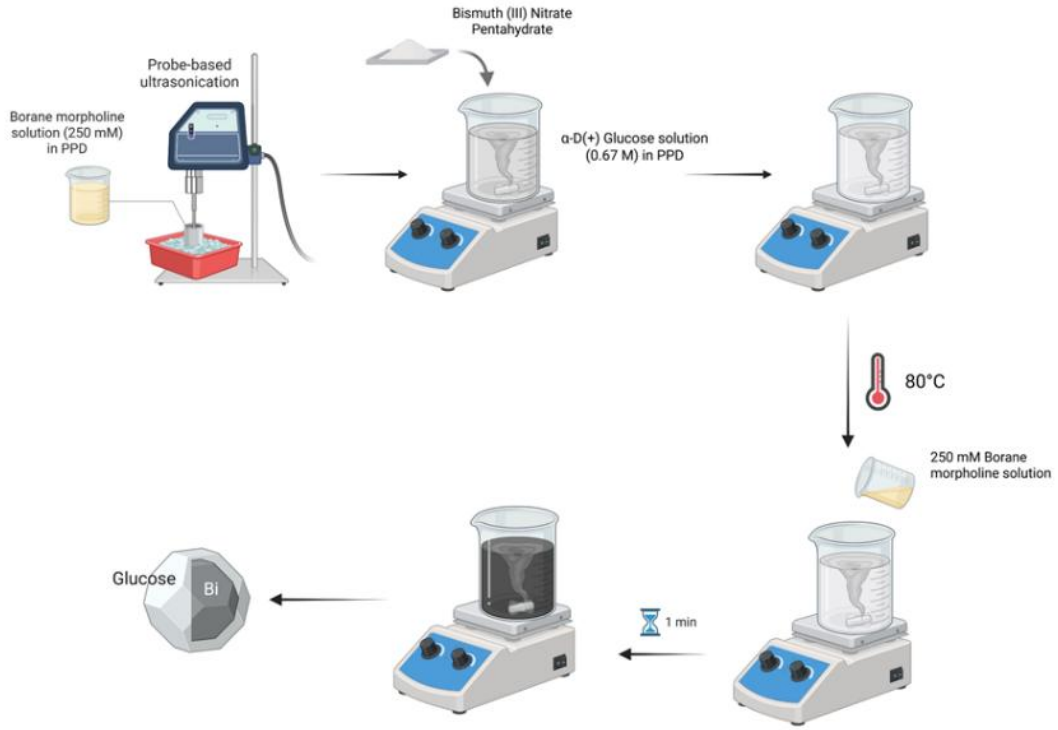

Figure 6: Picture of Bi Nps synthesis according to Li's protocol

Firstly, 20 g of α-D(+)-glucose, 0.970 g of bismuth (III) nitrate pentahydrate and 0.616 g of borane morpholine complex were accurately weighed using a digital precision balance.

Bismuth (III) nitrate pentahydrate was added to glucose powder and both completely dissolved in 175 mL of PPD into a three-necked round flask. To completely dissolve glucose and bismuth(III) nitrate Pentahydrate in PPD, the plate temperature was set

to 200 °C and the solution was kept under stirring condition at 1000 rpm for 45 minutes. With the support of the reaction thermometer, it was ensured that the temperature of the solution never exceeded 80°C. In the meantime, Morpholine Borane was dissolved in 24.4 mL of PPD in a 25 mL beaker, stirring the solution at 1500 rpm and warming it up to 80°C as well for 20 minutes.

Once the solution of glucose and bismuth reached the reduction temperature at 80 °C and no crystals were still visible, the morpholine borane solution was added all at once. The solution gradually changed color from clear to black, indicating the reduction of bismuth (III) ions to metallic bismuth (0), resulting in nanoparticles formation. The reaction was quenched exactly after 1 minute, in a 200 mL ice-cold Milli-Q water bath and allowed to cool to room temperature taking ~5-10 minutes.

Nanoparticles Purification:

After quenching the reaction, the particle suspension was further diluted with 200 mL of MilliQ water at room temperature and transferred into 50 mL Centrifugal tubes for centrifugation at 3,000 rcf for 1 hour to separate the pellet from the supernatant. The collected pellets were then combined and subjected to a purification process consisting of three consecutive centrifugation steps. After each centrifugation, the pellet was resuspended in the same initial volume of MilliQ water to ensure consistency. Three different centrifugation settings were tested for this purification step: 12,000 rpm for 20 minutes[48], 3,000 rcf for 30 minutes[46] and 3,000 rcf for 1 hour. The effectiveness of this approach was compared with dialysis-based purification, applying the previously optimized parameters from the earlier synthesis protocol.

Finally, although the original protocol did not include a filtration step, it was carried out in certain specific synthesis further discussed in the results to evaluate whether the synthesized particles could pass through the filter and to assess the effectiveness of the purification process. Finally, aqueous Bi Nps are stored at 4°C for future characterizations.

2.1.3 Brown vs Li Experimental Steps Comparison

In summary, two synthesis methods for bismuth nanoparticles were optimized, both using the same precursors. The main differences between the two approaches concern the amount of glucose used as a surfactant and its degree of dissolution in the common solvent. In Brown's protocol, glucose is used at a saturated concentration (3.57 M), resulting in only partial dissolution; therefore, Bismuth (III) Nitrate Pentahydrate must be dissolved separately in PPD, to ensure a full dissolution, before being added to the mixture. In contrast, Li's protocol uses a lower amount of glucose (0.66 M), which is mixed directly with bismuth precursor powder, allowing both precursors to fully dissolve in the common solvent.

Nanoparticles Lyophilization:

After comparing the two synthesis methods through morphological characterization, the particles deemed most suitable for the subsequent functionalization steps were lyophilized. Lyophilization (or freeze-drying) is a low-temperature drying technique used to remove water from nanoparticles while preserving their structure and long-term stability. This process allows the nanoparticles to be stored for extended periods and facilitates accurate weighing.

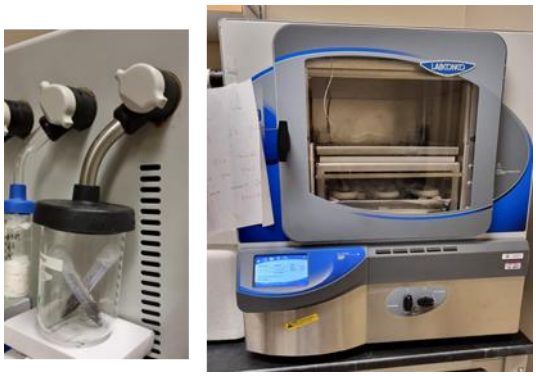

Figure 7: Picture of the used Freeze-dryer machine *(FreeZone Triad Freeze Dryer, Labconco Corporation, Kansas City, MO, USA)*

Briefly, the nanoparticles in aqueous suspension are rapidly frozen by placing them in a freezer at -80 °C for 24 hours, during which they become immobilized within the frozen matrix. They are then transferred to a freeze-dryer (FreeZone Triad Freeze Dryer, Labconco Corporation, Kansas City, MO, USA) (Figure 7), where the pressure is reduced to 0.016 Torr (0.02 atm) and the collector is maintained at -83.5 °C for an additional 24 hours. During this stage, the ice sublimates, leaving behind a dry and stable nanoparticle powder. The lyophilized nanoparticles are first weighed and then stored at 4 °C for future use.

2.2 Functionalization of Bismuth Nanoparticles

Synthetized Bi Nps were functionalized using a modified layer-by-layer (LbL) coating approach, following a protocol as described by Li *et al.*[47]. The LbL approach involved the sequential deposition of alternating polyelectrolyte layers, poly(allylamine hydrochloride) (PAH) and poly(acrylic acid) (PAA), and Amino-PEG-Acid (NH_2-PEG-COOH), onto particles surface. The addition of PEG provided colloidal stability and exposed reactive carboxyl groups (-COOH) for further bioconjugation Figure 8.

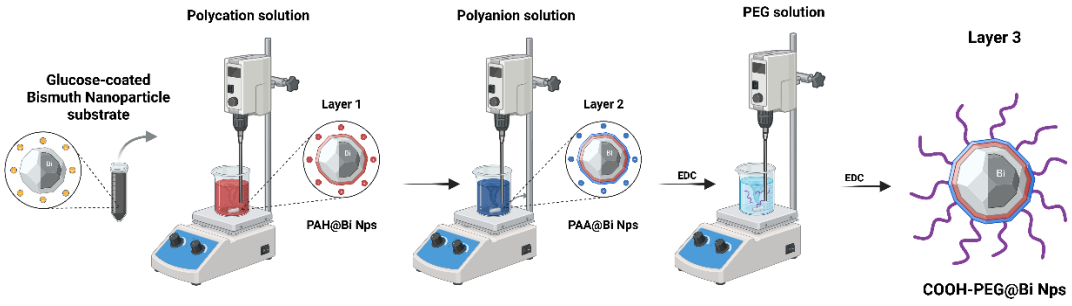

Figure 8: Schematic representation of Bi Nps functionalization process

Initially, lyophilized Bi Nps were resuspended in Milli-Q water at final concentrations of 1 mg/mL and 0.5 mg/mL. Aqueous PAH solutions were prepared at concentrations of 0.5 mg/mL, 1 mg/mL, and 1.5 mg/mL. The resuspend Bi Nps were added dropwise into the PAH solution under ultrasonication (Q55 Sonicator, Qsonica, Newtown, CT, USA) (Amplitude: 5-10, Mode: Continuous) and vigorous stirring for 30 minutes at 650-700 rpm. The coating process was performed at different ratios between the nanoparticles and the PAH solution to evaluate which condition yielded the most stable and efficient surface functionalization:

- [Bi Nps] = 1 mg/mL, [PAH] = 0.5 mg/mL → ratio 2:1
- [Bi Nps] = 1 mg/mL, [PAH] = 1 mg/mL → ratio 1:1
- [Bi Nps] = 0.5 mg/mL, [PAH] = 1 mg/mL → ratio 1:2
- [Bi Nps] = 0.5 mg/mL, [PAH] = 1.5 mg/mL → ratio 1:3

The suspension of PAH-coated Bi Nps (PAH@Bi Nps) was centrifuged at 3,000 rcf for 30 minutes to remove excess reagents, and the resulting pellet was resuspended in Milli-Q water to a final concentration of 1 mg/mL.

To apply the second polyelectrolyte layer, PAA solutions were prepared at different concentrations: 0.5 mg/mL, 0.8 mg/mL, and 1 mg/mL. The PAH@Bi NPs suspension was then added dropwise into the PAA solution under continuous ultrasonication and vigorous stirring using the same settings previously described. As with the first layer, the coating was performed at different nanoparticle-to-polymer mass ratios to identify the optimal conditions for stable and reproducible PAA deposition:

- [PAH@Bi Nps] = 1 mg/mL, [PAA] = 0.5 mg/mL → ratio 2:1
- [PAH@Bi Nps] = 1 mg/mL, [PAA] = 0.8 mg/mL → ratio 1:0.8
- [PAH@Bi Nps] = 1 mg/mL, [PAA] = 1 mg/mL → ratio 1:1

The suspension of PAA-coated Bi Nps (PAA@Bi NPs) was centrifuged at 3,000 rcf for 30 minutes to remove excess reagents, and the resulting pellet was resuspended in PBS (pH 7.4) to a final concentration of 1 mg/mL.

To induce covalent crosslinking between the PAH and PAA layers on the nanoparticle surface, EDC powder was added to the suspension to a concentration of 1 mg/mL. The mixture was ultrasonicated for 1 minute using the probe Sonicator (Amplitude: 5-10, Mode: Continuous) and then vigorously stirred for 1 hour (600 rpm) at room temperature.

Finally, NH_2-PEG-COOH (4 mg/mL) and EDC (2 mg/mL) powders were added into the PAA@Bi Nps dispersion upon ultrasonication for 10 min, and the reaction was allowed to stir overnight at room temperature. The final PEGylated Bi Nps (COOH-PEG@BiNps) were purified by centrifugation to remove excess reagents and subsequently resuspended in PBS.

2.3 Characterization of Bismuth Nanoparticles

To achieve a comprehensive characterization of the synthesized nanoparticles, several analytical techniques were employed, each targeting specific features of the formulated Bi NPs. Many physicochemical characterization techniques were performed using Dynamic Light Scattering (DLS) to determine the hydrodynamic diameter and polydispersity index, Zeta Potential analysis to assess colloidal stability by measuring surface charge, and Fourier Transform Infrared Spectroscopy (FT-IR) to qualitatively identify functional groups on the nanoparticle surface. Structural characterization was carried out via Transmission Electron Microscopy (TEM), which provided detailed information on particle morphology, core size, and size distribution. UV-Vis spectroscopy was used to evaluate optical absorption properties. The Inductively Coupled Plasma Optical Emission Spectroscopy (ICP-OES) technique enabled quantification of the elemental bismuth content. Finally, the effectiveness of the nanoparticles as imaging contrast agents was evaluated through micro-Computed Tomography (microCT), a functional characterization technique relevant for diagnostic applications.

Below is a detailed description of the characterization techniques used and how they were performed.

2.3.1 Size Distribution through Dynamic Light Scattering

Characterization using Dynamic Light Scattering (DLS) (ZETASIZER ADVANCE PRO, software ZS Xplorer, Malvern Panalytical) is a technique primarily used to determine the size distribution of particles in suspension, and when performed on the same formulation over time, it can assess the stability of suspended particles[59].

Figure 9: Picture of the used Dynamic Light Scattering device (*DLS) ZETASIZER ADVANCE PRO, software ZS Xplorer, Malvern Panalytical)*[60]

A highly collimated laser beam passes through the cuvette containing the nanoparticle suspension, which, due to Brownian motion, scatters the incident laser light in all directions, producing light scattering. A detector records this scattering. The data collected by the detector is processed using a temporal correlation function, which measures how quickly the intensity of the scattered light changes over time, determining the diffusion coefficient. The fluctuations in the scattered light intensity over time reflect the random movement of the particles: smaller particles move faster and cause rapid variations in the scattered light, while larger particles move more slowly and cause slower fluctuations. Using the diffusion coefficient obtained from the correlation function, DLS applies the Stokes-Einstein equation to calculate the hydrodynamic diameter.

$$D = \frac{\mathrm{kBT}}{6\pi\eta\mathrm{R}}$$

where D is the diffusion coefficient, k_B is the Boltzmann constant, T is the absolute temperature, η is the solvent viscosity, and R is the hydrodynamic radius.

To determine the hydrodynamic diameter and the size distribution of the synthesized nanoparticles,

1 mL of the sample was prepared into a cuvette (ZEN0040, Malvern Panalytical) in a 1:50 dilution ratio. Each sample is run in triplicates, setting Absorption index 2.988 and Refractive index 2.145[61].

The outcome of a DLS measurement is typically presented as a graph displaying the particle size distribution. Alongside the graph, the instrument provides key numerical data, including the average hydrodynamic diameter, offering a first estimate of particle size, and the Polydispersity Index (PDI), which reflects the degree of size uniformity within the sample. A PDI value below 0.2 generally indicates a monodisperse population, where the reported average size closely represents the dominant particle fraction. In contrast, a PDI above 0.2 suggests a polydisperse colloidal system, meaning a broader and more heterogeneous size distribution.

2.3.2 Surface Charge Evaluation through Zeta Potential

The Zeta Potential characterization measures the surface charge of particles in suspension, providing important information about their colloidal stability[59]. Charged particles in a fluid attract oppositely charged ions, forming an electric double layer. The zeta potential measures the electric potential at the interface between the Stern layer (where ions are tightly bound to the particle surface) and the more diffuse layer. It serves as an indicator of the electrostatic repulsion between particles, which determines whether they remain dispersed or tend to aggregate.

The measurement occurs by applying an electric field to the suspension (electrophoresis), causing the charged particles to move. The results are displayed in a graph showing the zeta potential distribution (x-axis in millivolts) compared to kcps (kilo counts per second), a unit that measures the intensity of light scattered by the particles during measurement, which reflects particle concentration and dispersibility within the sample.

The dispersant used in the sample is essential for zeta potential measurement, as it influences the system's electrical conductivity. Conductivity is related to the presence of ions in the dispersant, which interact with the electric field and the double layer around the particles. High conductivity can shield the electric field, reducing the measured zeta potential . On the other hand, low conductivity may affect measurement accuracy.

For this measurement, 1 mL of sample was prepared into a cuvette (DTS1070, Malvern Panalytical) by diluting sample to a 1:50 ratio. To make the dispersant electrically conductive enough so that a signal can be properly read, a 9% PBS (Phosphate Buffered Saline) MilliQ water solution was prepared and used as dispersant.

Based on the outcome of the characterization, the stability of the particles in suspension will be assessed: specifically, particles tend to aggregate and settle, and if this phenomenon occurs slowly, the suspension will be more stable. In such cases, the surface charge will have values far from neutral (very high positive or negative values). However, if this phenomenon occurs rapidly, the suspension will be less stable, and the surface charge will have values closer to zero.

2.3.3 Nanoparticles Chemical Stability Assessment through Ultraviolet/Visible Spectroscopy

Ultraviolet/Visible Spectroscopy (Cary 60 UV-Vis Spectrophotometer, Agilent Technologies, software Cary WinUV) is used to measure the absorption of ultraviolet

and visible radiation by a sample[62]. The absorption is associated with the excitation of electrons from their ground state to an excited state. Since the energy levels of matter are quantified, a specific wavelength is absorbed only if it has an associated energy that can cause an electronic transition.

Figure 10: Picture of the used UV-Vis Spectrophotometer (*Cary 60 UV-Vis Spectrophotometer, Agilent Technologies)*[63]

The light source of a UV-Vis spectrophotometer consists of a combination of a tungsten lamp, that emits in UV field (200-400nm) and deuterium ones that emits Visible light (400-800nm), which provide a beam of visible and ultraviolet radiation.

The principle underlying UV-Vis spectroscopy involves a light beam passing through a monochromator, which separates the light into its constituent wavelengths using a diffraction prism. This allows the selection of a specific (monochromatic) wavelength that will be directed through the sample, appropriately diluted in a dispersant. The cuvette containing the sample is made of quartz or glass, ensuring transparency to UV-Vis radiation.

When the light passes through the sample, depending on its chemical nature, concentration, and the thickness of the cuvette (typically 10 mm), part of the light is absorbed while the remainder is transmitted. The transmitted light reaches a detector, which converts its intensity into an electrical signal, measuring two primary intensities: I_o, the intensity of the incident light, and I, the intensity of the transmitted light after passing through the sample. The instrument calculates the absorbance (A) using the Lambert-Beer law:

$$A = \log_{10} \frac{I0}{I} = \varepsilon * c * l$$

Where **A** is sample absorbance, **ε** is the molar extinction coefficient, **c** is sample's concentration and **l** is the light path.

Finally, the spectrophotometer software records the absorbance (A) values for each wavelength. These are then plotted on a graph, where the X-axis represents the wavelength range (typically between 200 and 800 nm), and the Y-axis represents the calculated absorbance values that are also related to sample's concentration. The result is a curve or UV-Vis spectrum, which graphically represents the distribution of radiation intensity as a function of wavelength.

To determine the absorption spectrum of the synthesized Bi Nps, inside an optically transparent cuvette (10mm Light Path, HellmaAnalytics), 2 mL of the sample, were prepared by diluting the sample in MilliQ water at a 1:20 ratio. This dilution was performed to ensure an optimal concentration for spectroscopic analysis.

First, the dispersant in which the sample is diluted is analyzed, serving as the Baseline. This step is essential because UV-Vis instruments can introduce unwanted signals, such as background noise, and because the dispersant itself may absorb light within the UV-Vis range, contributing to the overall signal. By measuring the dispersant alone and subtracting its absorbance, the system is normalized, in a way that the dispersant's contribution is removed, leaving only the signal generated by the sample. This process ensures that the data reflects only the absorption peak of the sample, free from external interference.

The resulting spectrum allows for the quantitative and qualitative analysis of the sample's chemical properties. More specifically, the analysis will focus on detecting the characteristic peak of bismuth nanoparticles, which is expected to appear around 468 nm[61]. This peak allows verification of the chemical integrity of the nanoparticles over time, as long as the same characteristic peak remains well-defined around the same wavelength value.

2.3.4 Elemental Analysis through Inductively Coupled Plasma Optical Emission Spectroscopy

Inductively Coupled Plasma - Optical Emission Spectrometry (ICP-OES) (5800 ICP-OES, software ICP-OES Expert Agilent Technologies) is an analytical technique used to determine the concentration of both metallic and non-metallic elements in a sample.

Figure 11: Picture of the used Inductively Coupled Plasma - Optical Emission Spectrometry *(ICP-OES) device (5800 ICP-OES, software ICP-OES Expert Agilent Technologies)* [64]

The core of the system is an inductively coupled plasma torch, powered by an electromagnetic field generated by a coil. The torch is filled with an inert gas, typically Argon. When this gas is excited by a high-frequency current, it forms plasma, a cloud of ionized gas that can reach very high temperatures (up to 10,000 K). The sample, usually in liquid form, is nebulized into tiny droplets and introduced into the plasma through a nebulizer. Inside the plasma, the high temperature vaporizes, atomizes, and ionizes the elements in the sample. The excited atoms and ions in the plasma release the energy gained during ionization as they return to their fundamental energy state. This energy is emitted as light, and the wavelength of the light is specific to the material in the sample.

The optical system of the ICP-OES, which works between UV and IR spectra (170-800nm), separates the emitted light into a spectrum using a diffraction grating. Then, a detector, usually a photomultiplier or CCD, measures the intensity of the light at

each wavelength. This intensity is proportional to the concentration of the elements according to Lambert-Beer's law

$$I = k * C$$

Where **I** is the intensity of light emitted at a certain wavelength, **C** is the concentration of the element in the sample, and **k** is a proportionality constant that depends on experimental conditions (such as nebulization efficiency, plasma power, and the selected wavelength).

Creating a calibration curve is a crucial step in ICP-OES analysis, as it allows the signal intensity emitted by an element to be associated with its corresponding concentration. To construct a calibration curve, reference standards are used, which are samples with known concentrations of the element of interest. Each reference standard is analyzed using ICP-OES. During the analysis, the plasma excites the atoms and ions in the sample, and the intensity of the emitted light is recorded for that specific concentration. The result of characterizing all the reference standards is called the "calibration curve," which relates the element concentration to the signal intensity. This relationship is typically linear and follows the standard equation of a line:

$$y = mx + q$$

Where y is the intensity of the emitted signal, x is the concentration of the element, m is the slope of the line, and q is the y-intercept.

Once the calibration curve is constructed, it is possible to characterize a sample of unknown concentration. Just like with the calibration standards, the sample is nebulized, introduced into the plasma, and the intensity of the emitted light is measured. The intensity recorded by the instrument is then compared to the previously obtained calibration curve using linear interpolation. Therefore, by knowing the intensity of the light emitted by the sample, it is possible to determine its unknown concentration. Using the equation derived from the calibration curve, the unknown concentration of the element can be calculated by solving the equation for x.

Preparation of Yttrium Internal Standard: During an ICP-OES analysis, fluctuations in instrument conditions may occur, such as plasma power variations, gas flow changes, or nebulizer instability. To correct for these fluctuations, an Yittrium internal standard is run in parallel with the sample, and the relative concentration is verified to be always the same at a specific wavelength, in a way that any variation in the yttrium response can be employed to adjust the results of other monitored elements.

The yttrium standard consists of an aqueous solution of MilliQ water with 0.2% nitric acid (Nitric Acid, TraceMetal™ Grade, Fisher Chemical™) and 1 ppm yttrium standard for ICP (Yittrium Standard for ICP, 1000mg/L, Sigma-Aldrich).

Preparation of Standard Diluent: The Standard Diluent is a solution commonly used as a diluent for the preparation of calibration standards and samples to be analyzed. The Standard Diluent consists of an aqueous solution of MilliQ water with 10% Hydrochloric Acid (Hydrochloric Acid, TraceMetal™ Grade, Fisher Chemical™) and 1% Nitric Acid.

Preparation of Calibration Standards: Calibration Standards are used to build a calibration curve, which correlates the element concentration (in ppm or ppb) with the signal intensity measured by the instrument (in cps, counts per second). This curve is used to convert signals from unknown samples into quantitative concentrations.

Nine calibration standards are prepared, consisting of Standard Diluent solutions with different concentrations of bismuth standard for ICP (Bismuth ICP Standard 1000ppm Bi in 3% HNO_3, Ricca Chemical). The stock bismuth standard for ICP has a concentration of 1000 ppm, and the calibration standards are prepared by serial dilutions according to the dilution formula:

$$C1 * V1 = C2 * V2$$

Where V1 represents the concentration and volume of the initial stock, and C2 and V2 represent the final concentration and volume of the individual calibration standard.

Table 1 shows the relative calculations necessary to prepare 9 Bismuth Standards in 50 mL Centrifugal Tubes at 9 different concentrations in ppm ranging from 0.1 to 50 ppm. Specifically, standards 9 to 5 were prepared using the 1000 ppm bismuth ICP standard solution as the starting stock, while standards 4 to 1 were prepared using standard 7 as the starting stock solution (Table 1).

Standard	C1 (ppm)	V1 (mL)	C2 (ppm)	V2 (mL)
Standard 9	1000	2.5	50	50
Standard 8	1000	1.25	25	50
Standard 7	1000	0.5	10	50
Standard 6	1000	0.25	5	50
Standard 5	1000	0.125	2.5	50
Standard 4	10	5	1	50
Standard 3	10	2.5	0.5	50
Standard 2	10	1.25	0.25	50
Standard 1	10	0.5	0.1	50

Table 1: Bismuth Calibration Standards: *Table showing the calculation made to prepare the Bismuth Calibration Standards to build the Calibration Curve for ICP-OES.*

Preparation of Aqua Regia: To analyze solid metal particles, such as bismuth nanoparticles, it is necessary to dissolve them since the sample needs to be nebulized. Aqua regia is a 1:3 mixture of nitric acid (HNO_3) and hydrochloric acid (HCl) used for the dissolutions of metals and digestion of tissues in the case of biological samples, allowing for a homogeneous solution that can subsequently be analyzed.

Bismuth Nanoparticles Samples Preparation: To quantify the elemental Bi content of Bi NPs formulation through ICP-OES, sample are prepared in triplicates into three separate, pipetting respectively 25 µL, 50 µL, and 100 µL from stored bismuth

nanoparticles. This approach helps prevent technical sampling errors that can occur when handling such small quantities and confirms that the measured amount of bismuth is independent of the volume sampled, further validating the monodispersity of the colloidal nanoparticle solution.

Each sample is then digested by adding 1 mL of aqua regia and allowing it to sit for 30 minutes. Finally, 3 mL of Standard Diluent is added to each tube to attenuate Aqua Regia corrosive strength and preserve machine's running lanes.

ICP Protocol Setup*:* After preparing the samples, the next step is setting up the machine. First, the elements to be quantified are selected: bismuth (Bi) is chosen as the "Analyte," using the two wavelengths that ensure minimal interference with other materials, which in this case are 222.821 nm and 223.061 nm[2]. Then, yttrium (Y) is selected as the "Internal Standard" at a wavelength of 371.029 nm[65]. The measurement conditions are set in "Axial" mode, as it is ideal for aqueous solution samples, such as a nanoparticle suspension.

During the construction of the calibration curve for ICP-OES analysis, two key control parameters were set to ensure its reliability: the correlation coefficient limit and the calibration error. Specifically, the minimum acceptable value for the correlation coefficient was set at 0.995, while the maximum allowed calibration error was fixed at 20%. The correlation coefficient measures the degree of linear relationship between the known concentrations of the standards and the signal intensity detected by the instrument; a high value indicates good linearity of the response. On the other hand, the calibration error, expressed as a percentage, represents the deviation between the theoretical concentration of each standard and the value calculated from the calibration curve. Setting these parameters ensures that the selected curve is both linear and accurate enough to provide a reliable basis for quantitative sample analysis.

Once the setup phase is complete, the characterization begins. The machine will first run the nine bismuth standards to construct the calibration curve and then proceed

with the samples. For each sample, the light intensity is detected, and this value is interpolated on the calibration curve to determine the concentration (in ppm). In parallel, the yttrium internal standard is also run for each standard and each sample, and it should always show concentration values around 1 ppm to validate each measure.

Data processing: All the raw data is exported as an excel file and further processed. Since the detected concentration refers to a volume that includes the sample, the addition of 1 mL of Aqua Regia and 3 mL of Standard Diluent, makes it necessary to multiply by the dilution factor, through the formula

$$C1 * V1 = C2 * V2$$

to calculate the actual concentration of the single replicate. In this formula, V1 is the initial volume of the replicate, C1 is the concentration of interest, C2 is the concentration measured by the instrument, and V2 is the final volume of the sample analyzed. For each of the two wavelengths, the average V1 value will be calculated from the three replicates. Once the two average values (one for each wavelength) are obtained, an additional average will be calculated, resulting in a single concentration value that represents both wavelengths. Since the instrument provides results in ppm, a conversion to mg/mL is required, considering that 1 ppm = 0.001 mg/mL. Finally, by multiplying the concentration value (in mg/mL) by the stock volume (in mL) of the nanoparticles stock, the mass of bismuth contained in the formulation can be determined.

ICP-OES is then used to estimate the yield of the synthesis, the amount of bismuth detected will be compared to the theoretical mass of elemental bismuth (Bi) calculated from the initial amount of bismuth nitrate pentahydrate weighed, which, according to the manufacturer's datasheet, contains 43% of pure bismuth. This, according to the formula:

$$\%Yield = \frac{Mass\ of\ elemental\ Bi\ detected\ by\ ICP-OES}{0.43 * mass\ of\ Bismuth\ Nitrate(III)Pentahydrate\ used} * 100$$

2.3.5 Morphological Characterization through Transmission Electron Microscopy

Among the imaging techniques used for the morphological characterization of nanoparticles, Transmission Electron Microscopy (TEM) FEI Tecani G2 F20, Thermo Fisher Scientific, Waltham, MA, USA with SerialEM software, Nexperion, Vienna, Austria), thanks to its high resolution, reaching the sub-nanometer scale, allows for the direct observation of particle size and shape, making it particularly suitable for morphological characterization of nanostructured materials[62].

Figure 12: ***Picture of the used Transmission Electron Mycroscope*** *(TEM) (FEI Tecani G2 F20, Thermo Fisher Scientific, Waltham, MA, USA with SerialEM software, Nexperion, Vienna, Austria)*[66].

The working principle of TEM is based on the interaction between a beam of accelerated electrons and a thin sample. The beam is generated by an electron source, typically a tungsten filament, and is focused through a series of electromagnetic lenses. The electrons pass through the sample placed in the central chamber, which operates under high vacuum to prevent unwanted scattering. The transmitted electrons are then collected by a detector, such as a CCD camera or a fluorescent screen, producing a high-contrast two-dimensional image.

As the electron beam passes through the sample, part of the electrons is absorbed, scattered, or transmitted, depending on the electron density and the atomic number (Z) of the material. Inorganic materials (such as metals, oxides, or semiconductors) contain atoms with higher atomic numbers and greater electron density, which scatter and absorb electrons more effectively, resulting in higher contrast in the TEM image. In contrast, organic materials (such as polymer coatings, PEG, PAA, or proteins) are composed of light elements (e.g., C, H, O, N), which interact weakly with the electrons and appear almost transparent or barely visible in TEM analysis.

In the specific case of Bi Nps coated with glucose, the inorganic bismuth core, characterized by a very high atomic number (Z = 83), interacts strongly with the electron beam and is expected to appear as a dark and well-defined structure in the TEM image. In contrast, the glucose coating, composed of light elements, is difficult to detect and appears transparent or poorly contrasted.

The sample preparation was carried out by pipetting 5 µL of the nanoparticle suspension onto a copper grid (Support Films, Carbon 400 mesh, Cu, 01844-F, TED PELLA, INC.), which was then left to dry at room temperature over night. Once fully dried, the grid was carefully inserted into the microscope holder and placed inside the TEM instrument. Operating under high vacuum, the instrument allows the electron beam (Power: 200 kV and Magnification: x 11.5k) to interact directly with the dry nanoparticle sample, providing high-resolution images of the inorganic core structure.

The size of the bismuth core of the nanoparticles was measured using ImageJ. The “Polygon” selection tool was used to manually define the regions of interest (ROIs) to better follow the actual contours of the nanoparticles, which often exhibited irregular shape. The Feret diameter was selected as the reference metric to measure the core size of the nanoparticles. This choice was made because the particles exhibit irregular and anisotropic shapes, and the Feret diameter, defined as the longest distance between any two points along the particle boundary, provides a more consistent and representative estimate of their true maximum dimension compared to circular-equivalent diameters.

2.3.6 Surface Functional Group Identification through Fourier Transform Infrared Spectroscopy

Fourier Transform Infrared Spectroscopy (FT-IR) (Nicolet 6700, Thermo Fisher Scientific, Waltham, Massachusetts, USA) is an analytical technique used to study the chemical composition and molecular structure of materials by exploiting the interactions between infrared radiation and the chemical bonds present in the sample[62].

Figure 13:Picture of the used Fourier Transform Infrared Spectrometer (FT-IR) *(Nicolet 6700, Thermo Fisher Scientific, Waltham, Massachusetts, USA)*[67].

The fundamental principle is that molecules, when irradiated with infrared light, selectively absorb specific wavelengths that correspond to the vibrational frequencies of their chemical bonds. Each type of bond vibrates in characteristic ways, typically stretching or bending, at well-defined frequencies. In the case of FT-IR, the spectral range typically spans from 4000 to 700 cm^{-1}, corresponding to the mid-infrared region.

The FT-IR instrument uses an interferometer, usually of the Michelson type, which modulates the IR radiation to produce a complex signal known as an interferogram. This signal is then mathematically converted into an interpretable spectrum via the Fourier Transform, from which the technique takes its name. When the IR beam interacts with the sample, specific frequencies are selectively absorbed by the functional groups present. These absorptions appear as characteristic peaks in a

spectrum, where the x-axis represents the wavenumber (in cm^{-1}) and the y-axis can represent either Absorbance or %Transmittance.

More specifically, %Transmittance refers to the percentage of IR radiation that passes through the sample without being absorbed and is defined as:

$$\%Transmittance = \left(\frac{I}{I0}\right) * 100$$

where I is the intensity of the transmitted radiation and I_0 is the intensity of the incident radiation (with no sample). In this format, the peaks are oriented downward, and the deeper the peak, the greater the absorption. The %Transmittance scale is generally used for qualitative analysis, as is typically employed to identify the presence of functional groups and qualitatively compare different spectra.

Solid samples were prepared by mixing a small quantity of lyophilized bismuth nanoparticles with potassium bromide (KBr) powder, an IR-transparent substrate. The mixture was then pressed to form a compact pellet, which was subsequently placed in the machine, analyzed in the FT-IR instrument, previous Background subtraction.

2.3.7 Radiopacity Assessment through MicroCT Imaging

X-ray attenuation properties of the synthesized BiNPs were assessed using microCT (SKYSCAN 1276, Bruker, Mannheim, Germany) to confirm their radiographic visibility and to compare their attenuation values, expressed in Hounsfield Units (HU), with those of commercially available ICAs.

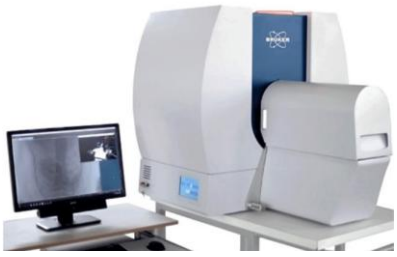

Figure 14: Picture of the used microCT scanner *(Bruker SKYSCAN 1276 CMOS Edition micro-CT (Bruker, Mannheim, Germany)*[68]*.*

Specifically, after quantifying the elemental bismuth (Bi) content in the Bi Nps formulation via ICP-OES, the nanoparticles were resuspended and serially diluted in MilliQ water to prepare a concentration range between 1 and 5 mg [Bi]/mL (1, 2, 3, 4, and 5 mg [Bi]/mL), in 0.5 mL centrifugal tubes. Solutions of ICAs were also prepared at the same concentrations in terms of iodine (1, 2, 3, 4, and 5 mg [I]/mL) by serial diluting a commercially available ICA solution Omnipaque 350 mg [I]/mL (Omnipaque™ (iohexol), GE HeathCare, Marlborough, MA, USA). Each sample was scanned using different tube voltages, 55 kV, 70 kV, 80 kV, and 100 kV respectively, to investigate how X-ray energy influences attenuation performance. The machine settings used for microCT scans are listed in Table 2: Protocols setup of microCT scan. Table showing the four different Protocols used to quantify the X-ray attenuation at different tube voltages of Bi Nps and traditional ICAs solutions.Table 2.

	Protocol 1	Protocol 2	Protocol 3	Protocol 4
Resolution (µm)	60	40	60	60
Matrix	504 x 336	1008 x 672	504 x 336	504 x 336
Exposure Time (ms)	60	135	60	60
Source Current (µA)	200	200	200	200
Tube Voltage (kV)	55	70	80	100

Table 2: Protocols setup of microCT scan*. Table showing the four different Protocols used to quantify the X-ray attenuation at different tube voltages of Bi Nps and traditional ICAs solutions.*

To determine whether Bi Nps offer superior radiopacity compared to ICAs, the attenuation values recorded at each concentration for the different imaging protocols were analyzed. After acquiring the microCT images, the first step involves importing the dataset in .dcm format into the software 3D Slicer (version). Once

uploaded, the three-dimensional volume is displayed in the orthogonal views: axial, coronal, and sagittal. The next step is segmentation, which allows the creation of a mask to isolate the region or material of interest from the background; this operation is performed on each of the three views of the sample. An intensity threshold is then applied to highlight only the portion of the sample located inside the centrifuge tube. The resulting 3D profile is then used to calculate the average attenuation (expressed in Hounsfield Units, HU) across the entire profile of each sample.

Subsequently, the tube voltage that resulted in the highest attenuation for ICAs was identified. Based on this setting, two curves were generated to compare the radiopacity of BiNPs and ICAs across the established concentration range, using the selected tube voltage. The obtained curves were compared to the baseline attenuation of cardiac tissue, at the same tube voltage. For this purpose, an *ex vivo* fragment of porcine heart tissue (Animal Technologies, Tyler, TX, USA) was freshly isolated and then stored in MilliQ water to ensure consistency with the dispersant used for both ICAs and BiNPs solutions.

3 Chapter 3 - Results & Discussion

3.1 Synthesis of high-payload bismuth-based nanoparticles

In this work, bismuth-based nanoparticles (Bi Nps) were synthesized by following and optimizing two already established protocols previously reported in the literature[46,48]. In both methods, Bi Nps were synthesized by dissolving bismuth (III) nitrate pentahydrate in 1,2-propanediol using α-D(+) glucose as a surfactant and borane morpholine as a reducing agent. After characterization, the two methods were compared to each other to determine the most suitable for the surface functionalization with PEG.

3.1.1 Brown's Protocol

3.1.1.1 Effect of Glucose degree of dissolution

The first aspect investigated was the degree of glucose dissolution in the Brown's protocol. Specifically, an attempt was made to completely dissolve the total amount of glucose in solution (specify amount), which required heating the mixture above the typical reduction temperature of 80 °C (*Figure 15*A). It was observed that dissolving this quantity of glucose required heating the solution to over 100 °C and stirring for approximately 4 hours (*Figure 15*B). Although the characteristic color changes from clear to black, associated with the reduction of bismuth(III) to bismuth(0), was observed during the reduction step, centrifugation resulted in an uneven precipitation of the pellet and complete separation from the surfactant phase (*Figure 15*C and *Figure 15*D). Furthermore, after purification by dialysis, the solid phase of the nanoparticles was found to be completely separated from the dispersant, leading to the formation of aggregates that subsequently precipitated (*Figure 15*E).

The outcome of this phenomenon is shown in *Figure 15*F, where DLS analysis indicates a hydrodynamic diameter of 991.2 ± 152.3 nm and a PDI of 0.70 ± 0.04. This behavior, known as “flocculation", is caused by poor interaction between the bismuth nanoparticles and glucose. It is likely that this instability was caused by the state of the glucose, because when mixed for too long and heated above 100 °C, it gets closer to its decomposition temperature of 142 °C, reducing its stabilizing ability as a capping agent.

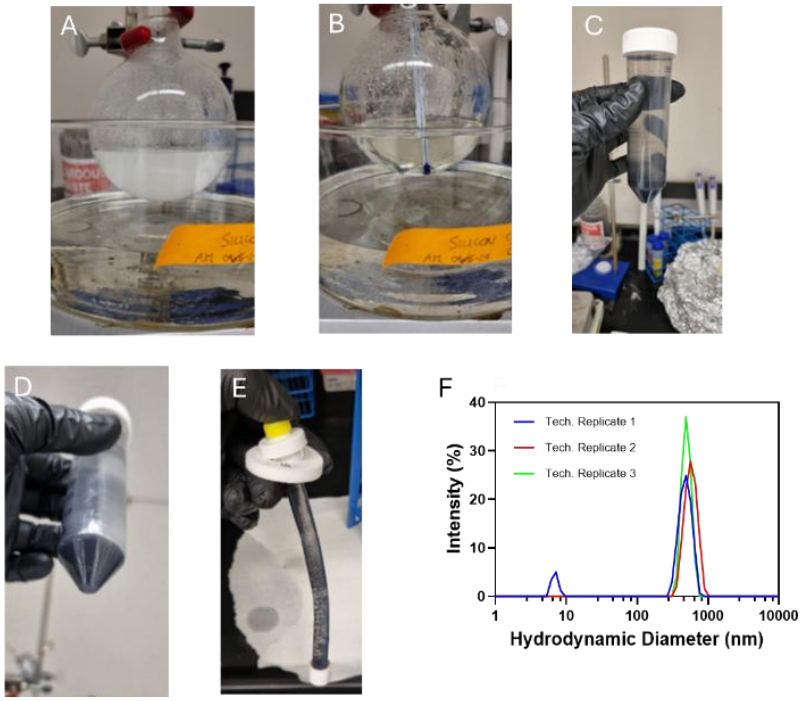

Figure 15: Evaluation of Glucose Solubilization and BiNps morphology after purification. *(A) Image showing the degree of glucose dissolution at 80°C, (B) Image of glucose completely dissolved at 100°C, (C) and (D) appearance of the Bi Nps pellet after centrifugation, (E) Contents of the dialysis membrane at the end of the purification process and (F) DLS spectrum of the flocculated particle samples run in triplicates.*

Thus, it was decided to dissolve the glucose only partially before initiating the reaction. Reaction was then initiated when the solution reached 80 °C following, as before, the steps described in the 2.1.1. *Figure 16*A shows the state of the nanoparticles in aqueous suspension at the end of dialysis: as illustrated, the particles remain homogeneously suspended. In contrast, *Figure 16*B displays the DLS spectrum

of the intact, non-flocculated particles, revealing a hydrodynamic diameter of 157.50 ± 5.02 nm and a PDI of 0.22 ± 0.01 for purified particles.

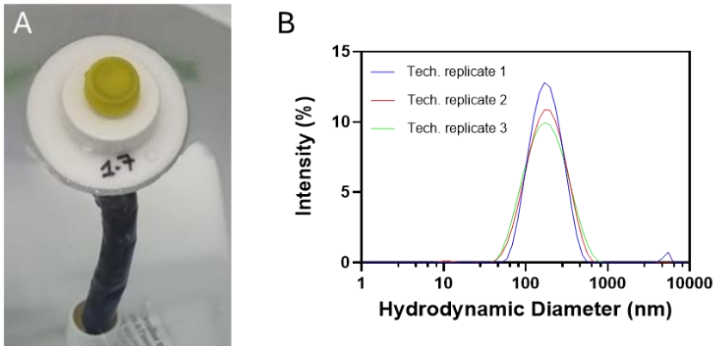

Figure 16: Evaluation of Bi Nps appearance and morphology after purification. *(A) Contents of the membranes at the end of the dialysis process. (B) DLS spectrum of purified Bi Nps homogeneously suspended, run in triplicates.*

3.1.1.2 Effect of pH

The effect of pH on the synthesis process was also investigated. Specifically, the standard MilliQ water, used for both quenching the reaction and dialysis, which had a pH of 4.5 (*Figure 17*A), was replaced with neutralized water where the pH was adjusted to 7–7.5 (*Figure 17*B), while all other protocol parameters were kept unchanged. The outcome of using neutralized water led to the formation of flocculated particles (*Figure 17*C).

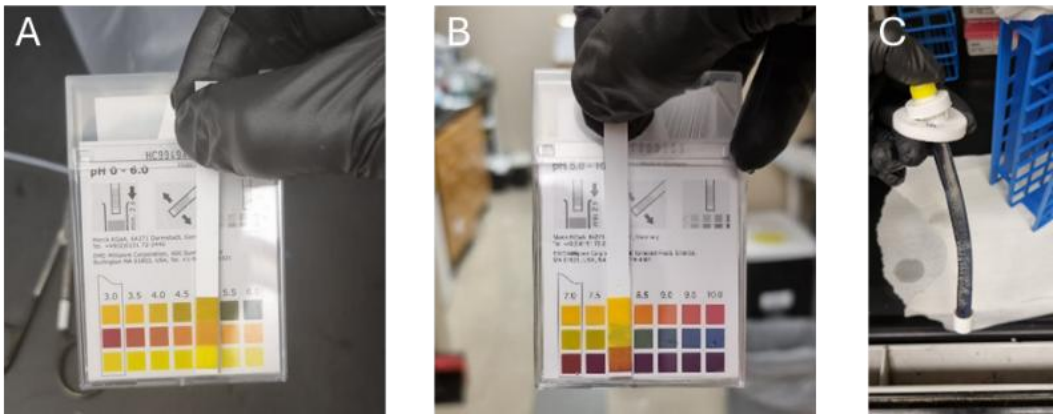

Figure 17: pH measurement of MilliQ water *(A) and (B) neutralized MilliQ water. (C) Flocculated particles at the end of the dialysis process.*

The flocculation observed when using neutralized water (pH 7–7.5) may be attributed to a reduced affinity of glucose for the particle surface during dialysis, which was also carried out using neutralized water as the dialysate. These conditions led to insufficient stabilization of the particles, resulting in flocculation. Therefore, standard acidic MilliQ water (pH 4.5) was reinstated in subsequent experiments, as it is stable particles in colloidal suspension.

3.1.1.3 Optimization of dialysis setup

The next step requiring optimization was the dialysis setup, as it was not described in details in the original protocol[46]. The initial configuration involved purifying the nanoparticles using 10 mL Float-a-Lyzer dialysis membranes, soaked in 5 L of MilliQ water (*Figure 18*A and *Figure 18*B). Although the nanoparticles appeared to remain homogeneously suspended at the end of the dialysis process, it was not possible to recover any after filtration. *Figure 18*C shows a comparison between a batch of unfiltered nanoparticles (left) and the corresponding filtered sample (right). As illustrated, the unfiltered suspension appears dark and concentrated, whereas the filtered suspension is almost clear, indicating a very low filtration yield. This suggests that a significant portion of the nanoparticles were retained by filter pores. An additional assessment of particle size was performed using Dynamic Light Scattering (DLS): *Figure 18*D shows a comparison between the DLS spectra of the unfiltered (S_NF) and filtered (S_F) samples. The analysis revealed a hydrodynamic diameter of 134.70 ± 1.93 nm for the unfiltered particles and 130.7 ± 2.82 nm for the filtered ones.

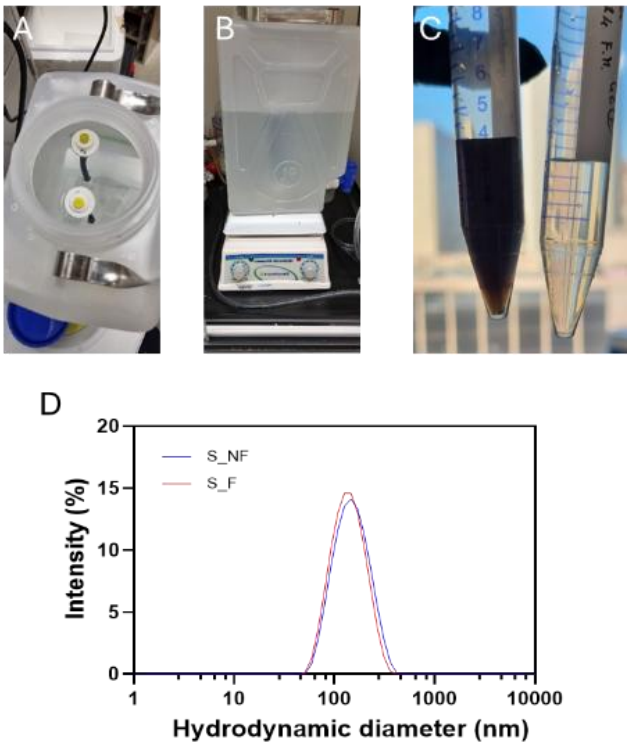

Figure 18: First Dialysis setup. *(A) and (B) Dialysis setup consisting of two 10 mL membranes filled and immersed in a 5 L MilliQ water-based dialysate. (C) Visual comparison between a batch of unfiltered particles (on the left) and filtered particles (on the right). (D) DLS spectrum of unfiltered nanoparticles (blue) and filtered nanoparticles (red).*

However, these results appear inconsistent with the visual observations. If the measured diameter of the unfiltered particles truly reflected their actual size, a higher filtration yield would have been expected. In that case, the filtered suspension should have resulted a darker appearance, as the particles would have been smaller than the nominal pore size of the filter (450 nm), and thus able to pass through without being retained. A possible explanation for this inconsistency is that the actual size of the unfiltered nanoparticles exceeded the upper detection limit of the DLS instrument. As a result, only a small fraction of the particles, those falling within the measurable range, may have been detected by DLS, leading to an underestimation of the true particle size distribution.

Thus, it was hypothesized that the possible explanation for the low filtration yield is linked to the dialysis setup. When using a large dialysate volume (5 L), the concentration gradient between the inside and outside of the membrane remains high, preventing equilibrium from being reached. As a result, diffusion continues

beyond the removal of excess reagents, gradually depleting even the glucose adsorbed on the nanoparticle surface. Since glucose acts as a stabilizer, its loss leads to particle destabilization and aggregation into larger structures, likely dimers or coalesce particles. Although the final suspension appears stable and dark by eye, the resulting aggregates likely exceed the filter pore size, preventing their recovery and explaining the clarity of the filtered solution.

Therefore, an alternative dialysis setup was tested, reducing the dialysate volume from 5 L to 1.5 L and using 1 mL Float-a-Lyzer membranes (*Figure 19*A) instead of 10 mL ones, while keeping the dialysis time unchanged. Figure 14B illustrates the visual comparison between the unfiltered (left) and filtered (right) nanoparticle suspensions, with the filtered sample further diluted to facilitate proper collection. Under these modified conditions, the filtration process yielded positive results, with nanoparticles successfully passing through the filter without being retained. Finally, *Figure 19*C shows the DLS spectra of unfiltered (S_NF) and filtered (S_F) particles. The analysis revealed a hydrodynamic diameter of 138.00 ± 0.89 nm and a PDI of 0.19 ± 0.01 for the unfiltered sample, while the filtered sample exhibited a diameter 125.60 ± 0.74 nm and a PDI of 0.19 ± 0.01. The filtration process allowed for better dispersion and separation of the particles, without significantly affecting the polydispersity. To further evaluate the colloidal stability of the synthesized nanoparticles, zeta potential analysis was performed on the filtered sample (S_F) to characterize their surface charge. As shown in *Figure 19*D, the zeta potential distribution indicates that the particles exhibit a surface charge of –-25.26 ± 1.94 mV.

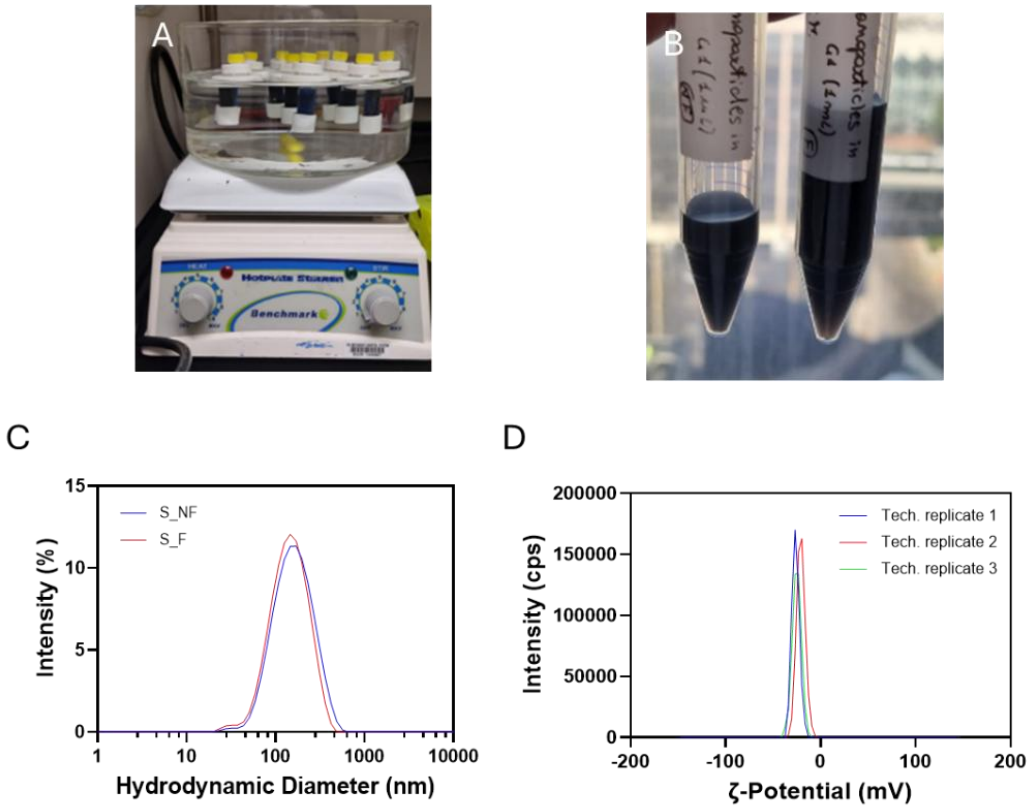

Figure 19: Improved Dialysis setup. *(A) Enhanced dialysis setup consisting of 1 mL membranes filled and immersed in a 1.5 L MilliQ water-based dialysate. (C) Visual comparison between a batch of unfiltered particles (on the left) and filtered particles (on the right). (D) DLS spectrum of unfiltered nanoparticles (blue) and filtered nanoparticles (red). (E) Zeta potential distribution spectrum of filtered BiNP samples run in triplicate.*

After optimizing the necessary steps to obtain a protocol capable of producing nanoparticles with stable colloidal suspension, the formulation was analyzed by TEM and then monitored over time to assess its long-term stability, using DLS, zeta potential, and UV-Vis spectroscopy. TEM images (**Error! Reference source not found.**A) showed that the resulting particles, composed of elemental bismuth, appeared faceted with variable shapes and diameters, with a bismuth core-size of 47.3 ± 14.26 nm. DLS analysis revealed a stable hydrodynamic diameter of 140.70 ± 14.77 nm and a PDI of 0.15 ± 0.04 (Figure 20B). UV-Vis spectroscopy exhibited a broad absorption peak between 380 and 400 nm, which remained stable over time with no significant wavelength shift (Figure 20**Error! Reference source not found.**C). Zeta potential measurements confirmed a consistent negative surface charge of –24.89 ± 0.94 mV for over 20 weeks (Figure 20D), indicating excellent long-term colloidal stability.

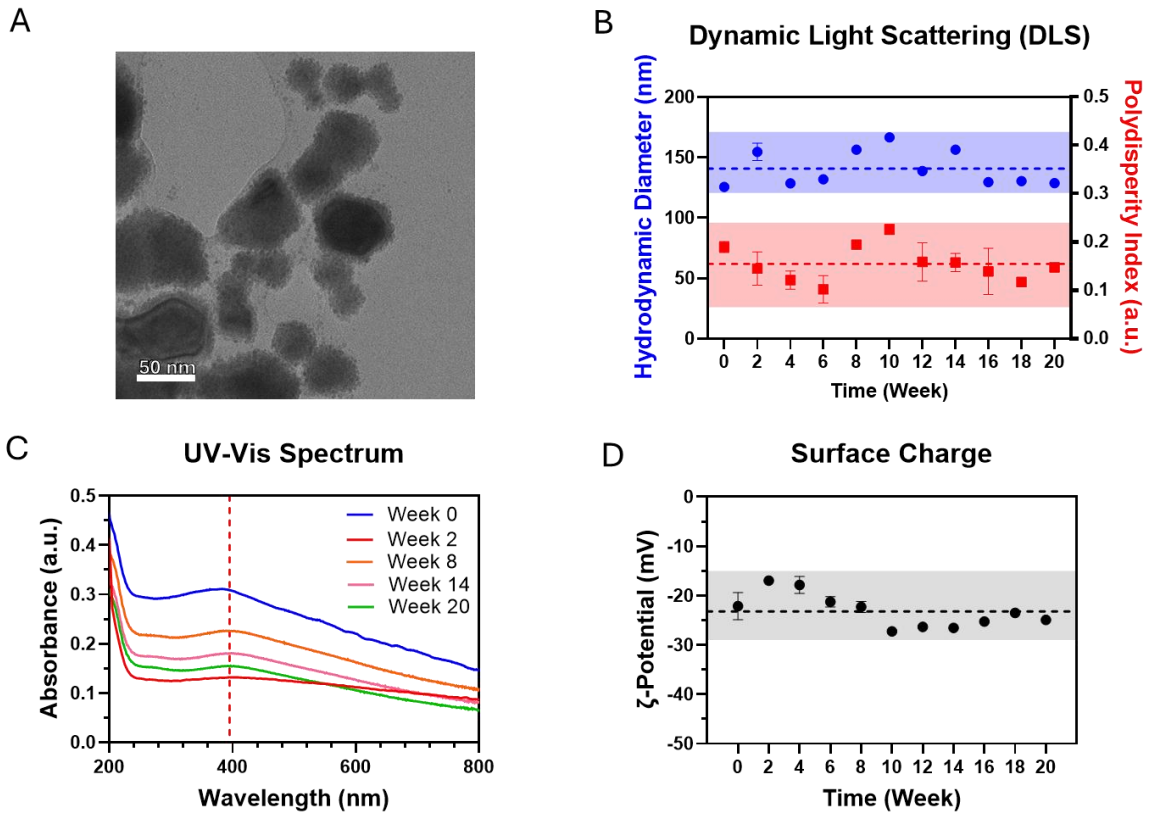

***Figure 20: C*aracterizations of synthesized BiNPs *following Brown's protocol*:** (A) TEM analysis showing the inorganic bismuth core (n=19). (B) Evaluation of hydrodynamic diameter (blue) and polydispersity index (red) over 20 weeks. (C) UV-Vis spectrum of synthesized BiNPs showing a broad absorption peak around 380 nm. (D) Evaluation of surface charge through zeta potential analysis over 20 weeks.

In conclusion, this synthesis protocol was carefully optimized through a series of iterative modifications involving reaction conditions, dialysis setup, filtration, and pH adjustment. This systematic approach enabled the successful formulation of bismuth nanoparticles with excellent colloidal stability in aqueous suspension. Notably, the final formulation remained stable for over 20 weeks, as confirmed by consistent hydrodynamic diameter, surface charge, and UV-Vis absorption profiles. These findings highlight the effectiveness of glucose as a stabilizing agent, capable of maintaining nanoparticle dispersion in water over extended periods.

3.1.1.4 Synthesis yield & optimization trials

Subsequently, the reaction yield was assessed by quantifying the amount of elemental bismuth (Bi) though ICP-OES. The results are expressed as the percentage of Bi recovered from the nanoparticle suspension at different stages of the synthesis, relative to the initial amount of bismuth precursor used. *Figure 21*A, B and C compares the Bi content in three steps of the synthesis: the Bi Nps suspension collected immediately after the quenching step (blue), the resuspended pellet obtained after centrifugation to separate it from the supernatant (green), and the Bi Nps suspension purified by dialysis (red).

To improve overall Bi yield, two variations of the original protocol were tested. In Variant 1 (*Figure 21*B), only the concentration of the reducing agent (Morpholine Borane) was doubled, resulting in a significantly higher final yield of ~44.08%, compared to ~2.97% for the original protocol (*Figure 21*A). In Variant 2 (*Figure 21*C), all reagents were doubled except for glucose, yet the final yield remained low (~3.05%). Importantly, the most significant bismuth loss consistently occurred during the centrifugation step, where the Bi content sharply decreased, for instance, from 76.84% to 2.97% in the original synthesis (*Figure 21*A) and from 92.58% to 3.05% in Variant 2 (*Figure 21*C), indicating that a substantial fraction of bismuth remains in the supernatant rather than forming recoverable nanoparticles.

Despite this improvement in material recovery for Variation 1, TEM analyses revealed significant differences in particle morphology. Nanoparticles obtained from the original protocol (*Figure 21*D) were more uniform in size and displayed well-defined, faceted shapes, consistent with controlled nucleation and growth. In contrast, particles synthesized via Variant 1 (*Figure 21*E) and Variant 2 (*Figure 21*F) appeared irregular in shape.

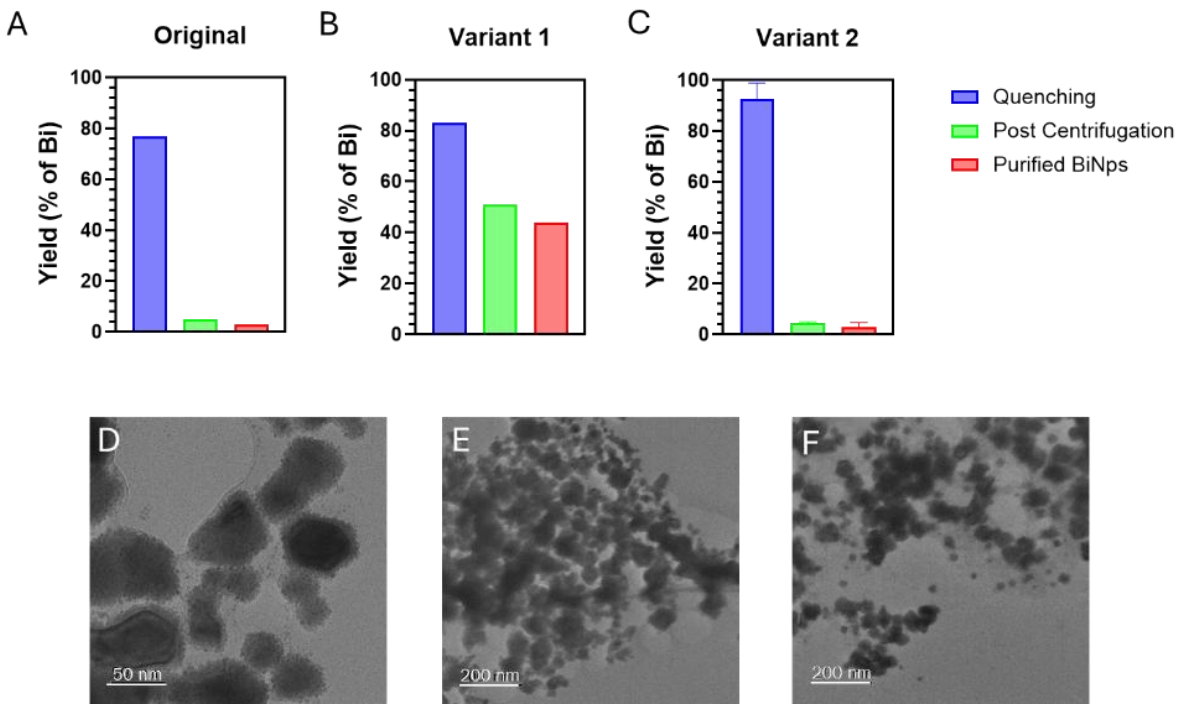

Figure 21: Evaluation of the yield percentage of synthesized BiNPs according to the Brown protocol *(A), doubling the concentration of the borane reducing agent (B) and doubling the amount of all reagents except glucose (C). TEM images of the particles from the corresponding syntheses are shown in (D) for the protocol in (A), in (E) for the protocol in (B), and in (F) for the protocol in (C).*

These results suggest that increasing reagent relative quantities may improve yield but compromise particle uniformity. Although Variant 1 led to a notable increase in the amount of elemental bismuth incorporated into the formulation, the original synthesis protocol was ultimately preferred, as it consistently produced nanoparticles with more uniform morphology. Moreover, a closer examination of the materials obtained from Variant 1 and Variant 2 (*Figure 21*E, *Figure 21*F) reveals that they do not contain well-defined nanoparticles, but rather irregular debris. This is likely attributable to the more aggressive reduction and rapid nucleation processes induced by the higher concentration of the reducing agent.

3.1.2 Li's Protocol

Briefly, the second method involves the use of the same reagents specifically, borane morpholine and bismuth nitrate pentahydrate, both maintained at a concentration of 250 mM. However, the glucose solution is less concentrated, at 0.66 M instead of 3.57 M as used in the first method. In this case, the bismuth and glucose solutions are dissolved simultaneously and completely[48].

3.1.2.1 Optimization of particles purification – Centrifugation vs dialysis

As previously described in the section 2.1.2, the purification protocol of the synthesized nanoparticles was optimized comparing three different centrifugation settings and dialysis. *Figure 22*A B, and C show the variation in hydrodynamic diameter and polydispersity index (PDI) of the nanoparticles, measured by dynamic light scattering (DLS), over the course of three successive centrifugation washes.

In the first condition tested (three times at 12,000 rpm for 20 minutes), the hydrodynamic diameter increased from 111.8 ± 1.01 nm and PDI 0.19 ± 0.06 after the first rinse to 178.50 ± 6.65 nm and PDI 0.41 after the third rinse (*Figure 22*A), indicating particles aggregation. Using a milder setting (3,000 rcf for 1 hour), the particles showed a diameter increase from 111.8 ± 1.01 nm and PDI 0.19 ± 0.01 after the first rinse to 206.8 ± 2.69 nm and PDI 0.17 ± 0.02 by the third rinse (*Figure 22*B). Finally, in the third condition (3,000 rcf for 30 minutes per rinse), the size increased from 108.5 ± 0.9 nm and PDI 0.20 ± 0.01 after the first rinse to 209.2 ± 9.25 nm and PDI 0.29 ± 0.16 after the third (*Figure 22*C).

Three different centrifugation protocols were initially tested to purify the nanoparticles by removing organic solvent residues and unreacted glucose through sequential washes. The first protocol (Figure 17A), adapted from a literature source[2], involved centrifugation at 12,000 rpm for 30 minutes but resulted in nanoparticle aggregation. To mitigate this, two additional conditions with reduced speed were evaluated. The second protocol (Figure 17B) lowered the speed to 3,000 rcf while increasing the duration to 60 minutes, and the third (Figure 17C) maintained the same reduced speed but halved the centrifugation time to 30 minutes. However, in

all cases, aggregation occurred, indicating that none of the centrifugation-based methods effectively preserved nanoparticle colloidal stability.

Given these results, purification was performed using the previously optimized dialysis protocol, which proved effective in maintaining nanoparticle stability. As shown in *Figure 22*D, the hydrodynamic diameter of Bi NPs remained consistent, with only a slight increase from 112.1 ± 0.50 nm and a PDI of 0.18 ± 0.01 before dialysis (S_Pre Dialysis) to 116.8 ± 2.55 nm and a PDI of 0.15 ± 0.01 after dialysis (S_NF), confirming minimal impact on particle size and distribution.

To further assess the effect of filtration on the dialyzed nanoparticles, a portion of the suspension was filtered. The filtration step did not alter the hydrodynamic diameter or PDI (S_F), confirming that the nanoparticles passed through the filter without aggregation. Based on these observations, filtration was excluded from the final protocol to prevent unnecessary nanoparticle loss due to inevitable small entrapment within filter pores of the particles, thereby maximizing material recovery for downstream applications.

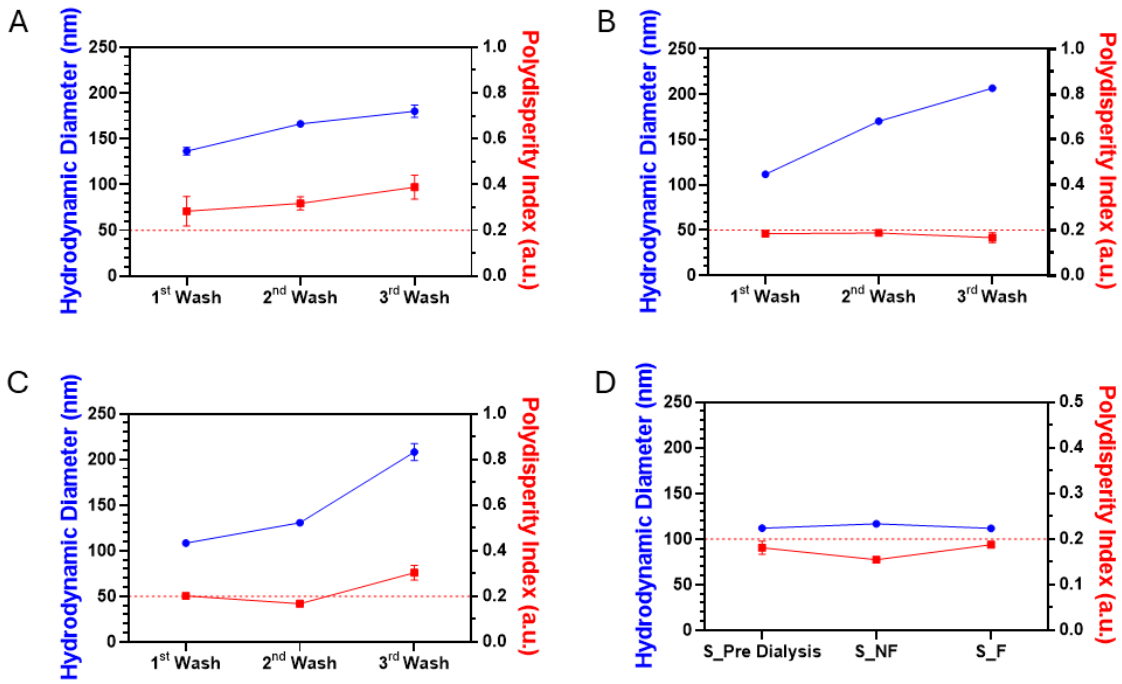

Figure 22: Variation of the hydrodynamic diameter (blue) and PDI (red) determined by DLS: *(A) Variation after each wash at 12,000 rpm for 30 minutes, (B) at 3,000 rcf for 1 hour, and (C) at 3,000 rcf for 30 minutes. (D) Variation before and after dialysis and after filtration of the Bi Nps.*

Following reaction yield assessment, Bi Nps were analyzed by TEM and characterized via DLS, zeta potential, and UV-Vis to verify long-term colloidal stability. *Figure 23*A shows a yield of 1.52%, with significant Bi loss during centrifugation, from 76.84% post-quenching to 2.97% post-centrifugation, due to unrecovered or unreacted bismuth in the supernatant. TEM (*Figure 23*B) images revealed uniform particles with a core size of 65.63 ± 9.64 nm. DLS and zeta potential analyses confirmed a hydrodynamic diameter of 107.8 ± 1.9 nm (*Figure 23*C) and a surface charge of -26.6 ± 1.7 mV (*Figure 23*D), respectively, indicating good colloidal stability over 20 weeks. UV-Vis spectra (*Figure 23*E) showed consistent absorption between 350–400 nm.

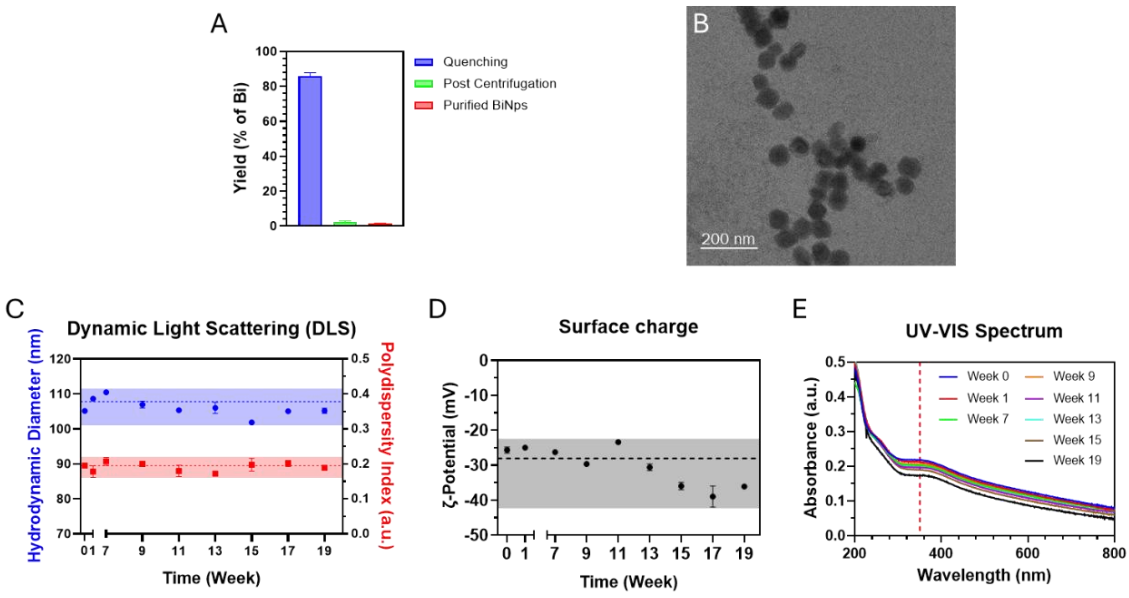

Figure 23:Outcome of Bi Nps synthesized according to Li's protocol: *(A) Evaluation of the yield percentage of synthesized Bi Nps according to Li's protocol. (B) TEM of synthesized Bi Nps (C) Evaluation of (C) hydrodynamic diameter (blue) and PDI (red) through DLS, (D) surface charge through zeta potential, and (E) UV-Vis spectrum over 20 weeks.*

3.1.2.2 X-ray attenuation

To evaluate the X-ray attenuation performance of the chosen Bi Nps, microCT scans were conducted and compared against commercial ICAs across a concentration range from 1 to 5 mg/mL. As shown in *Figure 24*A and *Figure 24*B, Bi Nps consistently exhibited higher attenuation values (HU) than ICAs at all tube voltages tested (55 kV, 70 kV, 80 kV, and 100 kV), according to the machine settings showed in Table 2. Results confirm superior radiopacity of bismuth-based materials due to their higher atomic number (Z = 83) compared to iodine (Z = 53).

After identifying 55 kV as the tube voltage that provides the highest attenuation in terms of HU for both samples set, this setting was selected for direct comparison between Bi Nps and ICAs attenuations using linear fitting. As shown in *Figure 24*C, the attenuation of both contrast agents increased linearly with concentration, indicating a proportional relationship between concentration and radiopacity. This resulted in two linear equations, for Bi and ICA, respectively:

$$Bi\ Nps: y = 163.0 * x + 585.5\ and\ ICA: y = 64.17 * x + 554.5$$

However, the slope of the linear fit for Bi Nps was markedly steeper than that of ICAs, reinforcing the greater X-ray attenuation capacity of bismuth under identical concentration ranges.

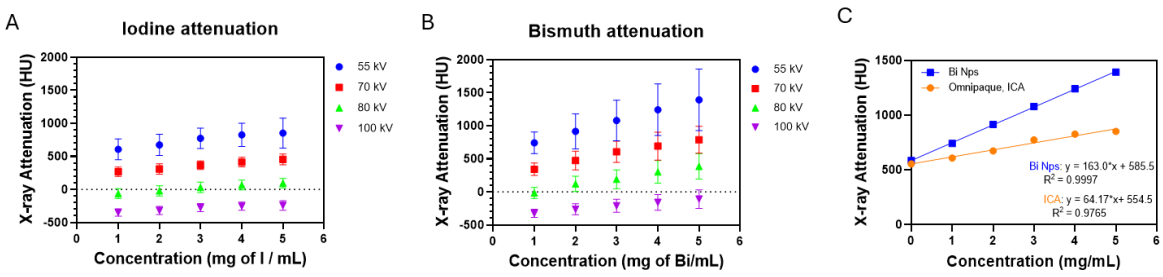

Figure 24: Evaluation of X-ray attenuation at different tube voltages *(55kV, 70kV, 80kV, and 100kV) for (A) elemental iodine (I) and (B) elemental bismuth (Bi) for synthesized Bi NPs. (C) comparison of X-ray attenuation between ICAs and Bi NPs at 55kV tube voltage.*

3.1.3 Optimization of Bi Nps Synthesis: Comparison of Brown and Li Protocols

I summary, were optimized two different synthesis protocols, from Brown *et al.*[46] and Li *et al.*[48], which employs the same reactants but with a reduced concentration of D-(+)-glucose, from 3.57 M to 0.66 M. Moreover, while Brown's method involves partial dissolution of glucose prior to the addition of the bismuth solution, Li's protocol include the bismuth directly to the glucose solution, allowing both components to dissolve completely together.

DLS and TEM analyses were employed to check differences: nanoparticles synthesized using Brown's method showed a hydrodynamic diameter of 140.70 ± 14.77 nm and a polydispersity index (PDI) of 0.15 ± 0.037 (Figure 20**Error! Reference source not found.**B), whereas those obtained using Li's method exhibited a smaller diameter of 106.35 ± 2.75 nm and a slightly higher PDI of 0.19 ± 0.01 (*Figure 23*). Despite this, nanoparticles produced by both methods remained stable in aqueous suspension for over 20 weeks, as confirmed by DLS, zeta potential, and UV-Vis analyses (Figure 20 and *Figure 23*), further validating the improved colloidal stability due to the glucose coating. Based on TEM images, the nanoparticles synthesized using Brown's protocol exhibited a smaller bismuth core size (47.3 ± 14.26 nm) compared to those obtained with Li's method (65.63 ± 9.64 nm), despite the latter showing a lower hydrodynamic diameter in DLS measurements. This suggests that nanoparticles produced via Li's synthesis may possess a higher bismuth payload and a thinner glucose shell. However, the particles synthesized via Li's method were more uniform in both size and morphology, indicating improved crystalline Figure 20A and *Figure 23*B).

Based on these findings, Li's method was selected for further nanoparticle functionalization due to its ability to produce Bi Nps with more controlled morphology

By the way, one of the main limitations of these syntheses is the poor stability of the glucose coating. As shown in the section discussing purification by centrifugation,

performing three washing steps caused the coating to break down, leading to particle aggregation (*Figure 22*). While dialysis can effectively purify the nanoparticles without affecting their shape or size, centrifugation is a faster method to obtain the final formulation. For this reason, further optimization of centrifugation conditions, in terms of speed and duration are needed. Another limitation is the low overall yield of the synthesis. In both the Brown and Li methods, the amount of elemental Bi measured was quite low, since most of the material remained in the supernatant (*Figure 21*A and *Figure 23*A). Therefore, it will be important to improve some steps of the synthesis, such as the reaction conditions or the centrifugation process used to separate the pellet from the supernatant and remove excess reagents.

3.2 Functionalization of Bismuth Nanoparticles

The next step involved the functionalization of the nanoparticles using a layer-by-layer (LbL) approach. After selecting the particles deemed most suitable for surface modification, a protocol adapted and optimized from the study by Li et al.[47] was followed. In brief, multilayer coatings were created by alternately depositing thin layers of a polycation, such as poly(allylamine hydrochloride) (PAH), and poly(acrylic acid) (PAA) as polyanion, prior to the addition of Amino-PEG-Acid (NH_2-PEG-COOH).

3.2.1 Layer-By-Layer Coating

As previously mentioned in Chapter 2, the Layer-by-Layer (LbL) protocol reported in the literature was optimized by testing different concentration ratios between Bi Nps and the selected polyelectrolytes. To verify the success of each coating step, DLS and zeta potential measurements were employed for each layer.

For the deposition of the first layer, the initial ratio tested was the one reported in the reference paper[47], corresponding to a 2:1 concentration ratio of Bi Nps to PAH,

and then was also tested the 1:1 ratio. *Figure 25* shows the corresponding DLS analysis, and the zeta potential values obtained for the nanoparticles. Both analyses revealed that the coating under these conditions was not effective, as no shift toward a positive surface charge was observed (*Figure 25*B and *Figure 25*D), nor was there any increase in hydrodynamic diameter (*Figure 25*A and *Figure 25*C), indicating that PAH did not successfully adsorb onto the nanoparticle surface.

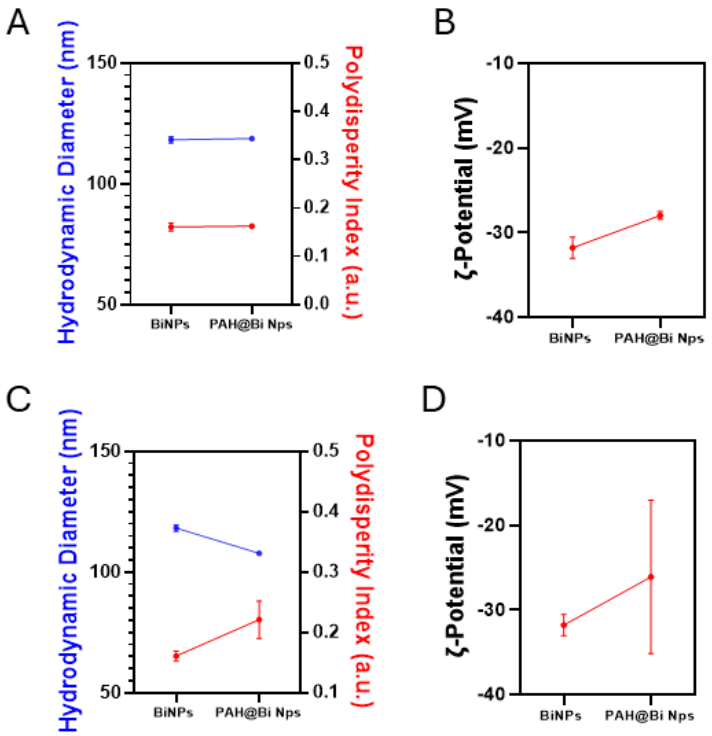

Figure 25: Outcome of PAH coating trials*: Evaluation of hydrodynamic diameter (blue) and PDI (red) through DLS, and surface charge through zeta potential analysis of: (A) and (C) hydrodynamic diameter and PDI for Bi NPs to PAH ratio 2:1 and 1:1, respectively, and (B) and (D) zeta potential for the same ratios*

Assuming that the failure of the coating was due to an insufficient amount of PAH, an higher quantity of polyelectrolyte was used to promote the formation of a more homogeneous and stable coating[69]. Therefore, the nanoparticles were resuspended at a lower concentration of 0.5 mg/mL, while PAH solutions were prepared at 1

mg/mL and 1.5 mg/mL, resulting in a ratio Bi Nps to PAH equal to 1:2 and 1:3, respectively.

As shown by zeta potential and DLS characterizations, the higher quantity of PAH in solution promotes effective coating of the nanoparticles through electrostatic interactions. Specifically, the zeta potential increased from – 31.8 ± 1.26 mV for the uncoated Bi Nps to +6.74 ±0.72 mV for PAH@Bi Nps when coated using a 1 mg/mL PAH solution (*Figure 26*B), and from –25.0 mV ± 0.69 to +19.27 ± 1.40 mV when using a 1.5 mg/mL PAH solution (*Figure 26*F). Similarly, the increase in zeta potential was accompanied by a rise in hydrodynamic diameter, from 107.8 ± 1.41 nm to 122.9 ± 1.64 nm for the first group (*Figure 26*A), and from 114.2 ± 0.46 nm to 134.4 ± 2.44 nm for the second group (*Figure 26*E), further confirming the successful attachment of the PAH coating.

However, when attempting to replicate the same conditions, it was observed that PAH coating using a 1 mg/mL solution was not consistently successful. In some cases, PAH@Bi Nps displayed unstable zeta potential values across technical replicates (*Figure 26*C) or showed positive values very close to zero (*Figure 26*D). This is likely because 1 mg/mL represents the minimum amount of PAH required to coat the particles, but not enough to do it homogenously.

Therefore, a Bi Nps to PAH ratio of 1:3 was adopted for further functionalization steps, as it provided a more distinctly positive surface charge, reproducible across the three replicates (*Figure 26*G), and a stable coating even after 24 hours (*Figure 26*H).

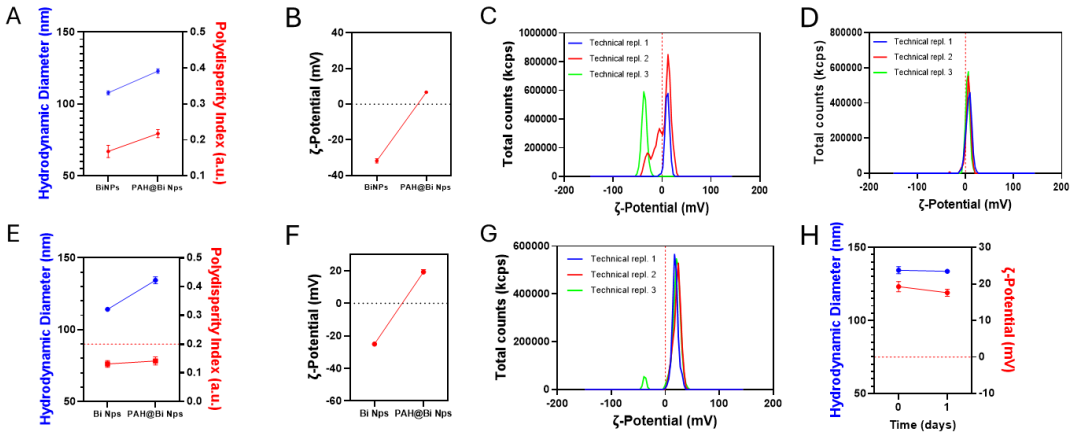

Figure 26: Outcome of PAH coating trials*: Evaluation of hydrodynamic diameter (blue) and PDI (red) through DLS, and surface charge through zeta potential analysis of: (A) and (E) hydrodynamic diameter and PDI for Bi NPs to PAH ratio 1:2 and 1:3, respectively, and (B) and (F) zeta potential for the same ratios. (C) and (D) Zeta potential distribution spectrum of PAH@Bi Nps for Bi NPs to PAH ratio 1:2 run in triplicates. (G) Zeta potential distribution spectrum of PAH@Bi Nps for Bi NPs to PAH ratio 1:3, run in triplicates. (H) Evaluation of PAH coating (1:3 ratio) stability over 24 hours through DLS (Blue) and Zeta potential (red) analyses.*

After confirming the stability of the PAH@Bi Nps, the coating process was further optimized by adding the next polyelectrolyte layer, PAA. As before, three different ratios between PAH@Bi NPs and PAA solution were tested. According to DLS and zeta potential analyses, the PAA coating was ineffective when using PAA solutions at concentrations of 0.5 mg/mL[47] and 0.8 mg/mL. In both cases, the PAA-coated nanoparticles (PAA@Bi Nps) showed a decrease in surface charge(*Figure 27*B and *Figure 27*D). The hydrodynamic diameter of PAH@Bi Nps further provided evidence of the unsuccessful layer addition with a decrease in value from 126.8 ± 1.07 nm to 117.3 ±1.40 nm for PAA@Bi Nps with 0.5 mg/mL PAA solution, to 116.2 ± 1.20 nm with 0.8 mg/mL PAA one. (*Figure 27*A and *Figure 27*C).

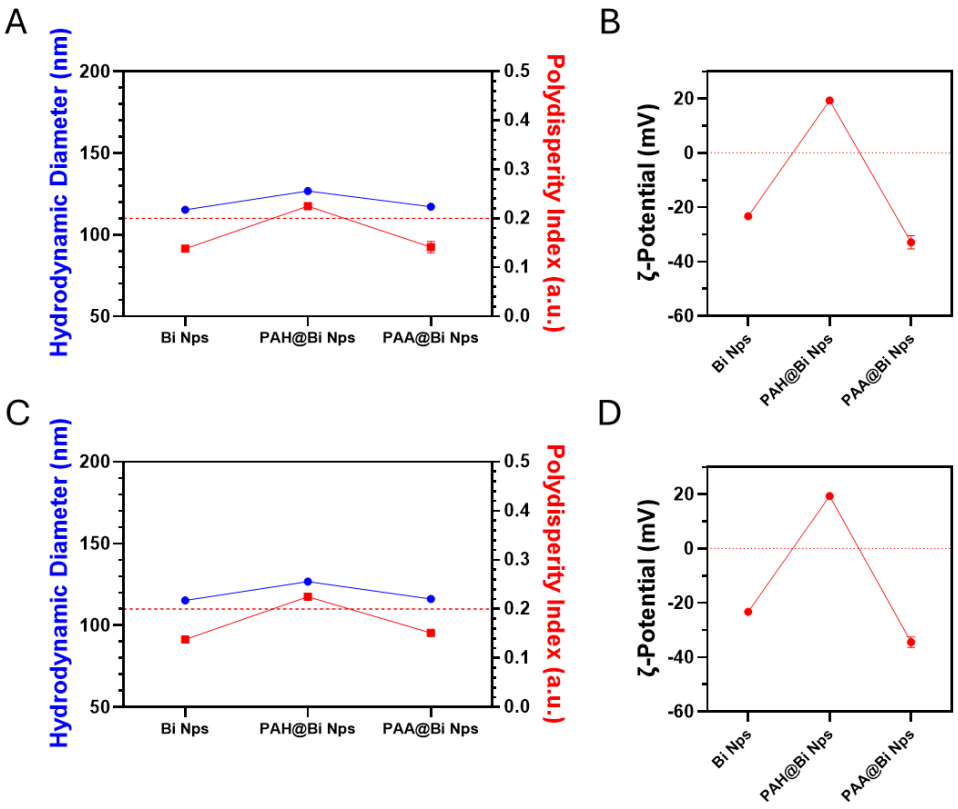

***Figure 27:Outcome of PAA coating trials**: Evaluation of hydrodynamic diameter (blue) and PDI (red) through DLS, and surface charge through zeta potential analysis of: (A) and (C) hydrodynamic diameter and PDI for PAH@Bi Nps to PAa ratio 2:1 and 1:0.8 respectively, and (B) and (D) zeta potential for the same ratios.*

In contrast, using a PAA concentration of 1 mg/mL resulted in a progressive increase in hydrodynamic diameter, from 126.6 ± 1.68 nm for PAH@Bi Nps to 142.9 ± 1.80 nm for PAA@Bi Nps (*Figure 28*A), maintaining also a PDI below 0.2. Also, the zeta potential shifted from +12.5 ± 0.54 mV for PAH@Bi Nps to –34.4 ± 1.72 mV for PAA@Bi NPs (*Figure 28*B).

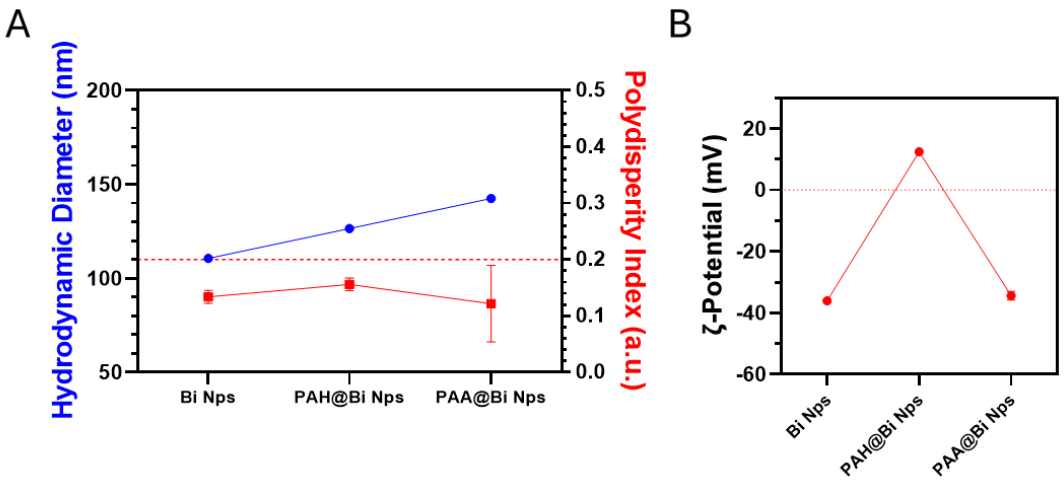

***Figure 28: Outcome of PAA coating trials**: (A) Evaluation of hydrodynamic diameter (blue) and PDI (red) through DLS, and (B) surface charge through zeta potential analysis for PAA@Bi Nps to PAA ratio 1:1.*

Regarding the optimization of the PEGylation step, no additional modifications were required compared to the already established protocol[47].

PEG-coated Bi NPs (COOH-PEG@Bi Nps) exhibit an increase in size from 142.9 ± 1.80 nm and PDI 0.12 ± 0.07 for the PAA@Bi NPs to 151.1 ± 0.49 nm and PDI 0.15 ± 0.03 for COOH-PEG@Bi Nps (*Figure 29*A). Similarly, the zeta potential shows a slight shift in surface charge from -34.37 ± 1.72 mV to -16.98 ± 0.57 mV for the same groups (*Figure 29*B).

To further confirm the presence of PEG on the surface of the nanoparticles, FT-IR analysis was performed on the three key components: uncoated Bi Nps, the pure NH_2-PEG-COOH, and the PEGylated nanoparticles (COOH-PEG@Bi Nps) (*Figure 29*C).

In the region between 3000 and 3500 cm^{-1}, all spectra display a broad band generally attributed to the stretching vibrations of –OH and –NH groups. Specifically, while in the spectrum of Bi Nps this peak is realted to the -OH groups of the glucose coating, the spectrum of free PEG shows a single broad peak due to the overlap of the O–H stretching from the carboxylic acid group and the N–H stretching from the terminal amine. However, in the PEGylated Bi Nps, the peak in this region likely corresponds

solely to the free carboxyil end, suggesting that the amine group is no longer free, having reacted during the conjugation process.

Another significant difference of PEG alone is observed between 2800 and 3000 cm^{-1}, which corresponds to the aliphatic -CH_2 stretching vibrations.

Particularly evident is the peak around 1100 cm^{-1}, which is associated with the stretching of ether bonds (C–O–C) in the PEG backbone. This signal is very intense in free PEG and remains visible, in the PEGylated BiNPs, further validating the presence of PEG on the nanoparticle surface.

In the region between 1700 and 1720 cm^{-1}, a peak attributable to the carbonyl (C=O) stretching of the free carboxylic acid group is observed. This band appears in both the free PEG and PEGylated Bi Nps spectra.

The presence of this peak with a new band between 1500 and 1600 cm^{-1}, absent in the other spectra and only present in PEGylated BiNPs, is particularly significant. This latter band is associated with N–H bending and C–N stretching vibrations.

Overall, the most relevant peaks found at 1100 cm^{-1} and 1700 cm^{-1}, serve as a markers to confirm the successful surface functionalization: the former indicating the presence of the PEG ether backbone on the nanoparticles, and the latter confirming the retention of a free carboxyl terminal group.

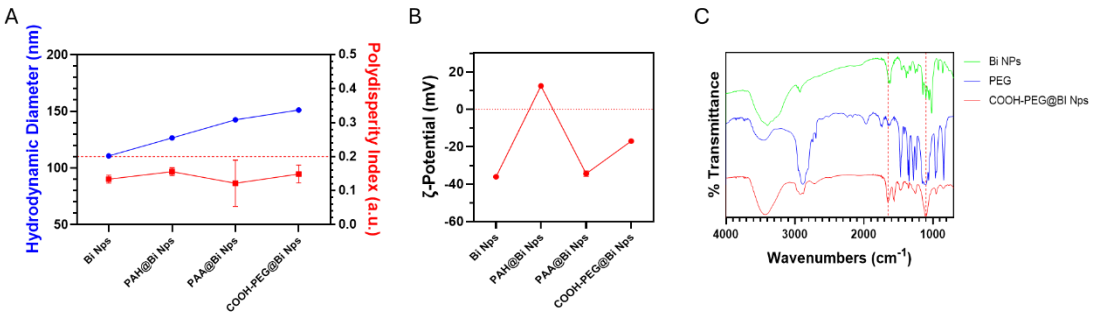

Figure 29: Surface functionalization evaluation of Bi Nps. *(A) Evaluation of hydrodynamic diameter (blue) and PDI (red) through DLS analysis across the whole functionalization process. (B) Evaluation of surface charge though Zeta potential analysis across the whole functionalization process. (C) FT-IR*

Spectra showing %transmittance as a function of wavenumber, to compare lyophilized Bi Nps (green), NH_2-PEG-COOH alone (blue) and PEGylated Bi Nps (red).

Finally, the stability of the PEGylation was evaluated by characterizing COOH-PEG@Bi Nps over a period of up to four weeks using DLS and zeta potential analysis. *Figure 30*A and *Figure 30*B demonstrate the stability of the PEG-based coating, showing an average hydrodynamic diameter of 148.24 ± 2.01 nm and a PDI of 0.15 ± 0.04, along with a consistently negative surface charge of -15.87 ± 1.05 mV.

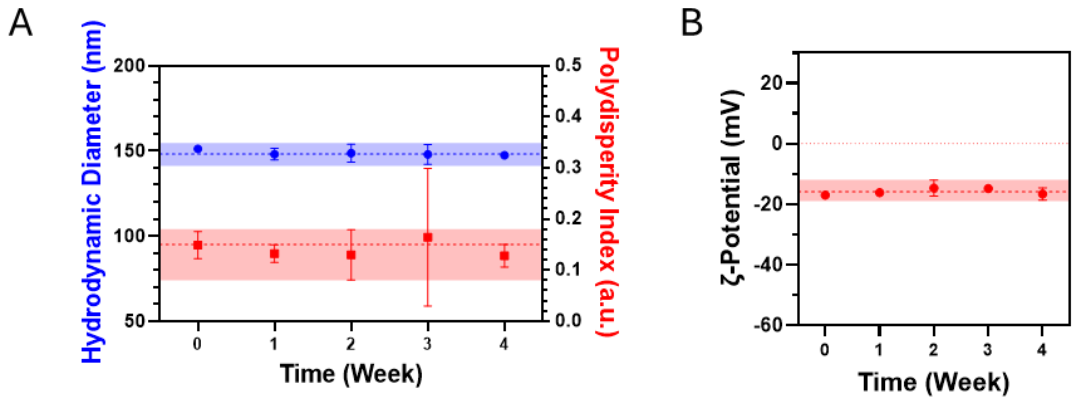

Figure 30: Assessment of PEGylated Bi Nps stability. *Evaluation of (A) hydrodynamic diameter (blue) and PDI (red) and (B) surface charge, over 4 weeks.*

3.2.2 Tailoring the Surface Chemistry of Bi Nps

The functionalization process of BiNPs required multiple optimization steps, as the protocol previously reported in the literature proved ineffective when applied to the nanoparticle formulation developed in this thesis. Therefore, the optimization focused on adjusting the relative amounts of each component, including the polyelectrolytes PAH and PAA, as well as the concentration of the BiNPs: after testing several ratios between BiNPs, PAH, and PAA, the combination that resulted in a stable coating was found to be 1:3:1, respectively for BiNPs, PAH, and PAA, in terms of

concentration. Regarding the PEGylation step, a key modification was necessary. The originally used methoxy-PEG-amine (mPEG-NH_2), bearing a terminal methoxy group, did not allow for further surface modification of the PEGylated BiNPs without complex chemical alterations that could compromise nanoparticle stability. To overcome this limitation, a heterobifunctional NH_2-PEG-COOH was selected. The amino end (-NH_2) enabled covalent attachment to the nanoparticle surface, while the free carboxylic group (-COOH) allowed for subsequent antibody conjugation.

Characterization by DLS and Zeta Potential analysis after each coating revealed a gradual increase in hydrodynamic diameter and a shift in surface charge. Specifically, as shown in *Figure 29* the hydrodynamic size increased from 110.3± 0.07 nm for uncoated BiNPs to 151.1 ± 0.49 nm for PEGylated BiNPs, while the surface charge shifted from – 36.3 ± 1.07 mV to -16.98 ± 0.57 mV, confirming the successful sequential deposition of each layer. Further confirmation of successful PEGylation was provided by Fourier-Transform Infrared Spectroscopy (FT-IR). The FT-IR spectra of PEGylated BiNPs showed characteristic absorption bands around 1100 cm^{-1}, corresponding to the PEG backbone (C–O–C) stretching, and around 1700 cm^{-1}, indicating the presence of carbonyl (C=O) groups, which are consistent with the carboxyl terminal group of the PEG.

Finally, unchanged DLS and zeta potential values over time, confirmed that the PEG coating provided colloidal stability in aqueous suspension for up to four weeks (*Figure 30*).

4 Chapter 4 - Conclusion

In this work, Bi Nps were successfully synthesized following two literature protocols, both using bismuth(III) nitrate pentahydrate as the salt precursor, morpholine borane as the reducing agent, and glucose as the stabilizer and capping agent, all in the common solvent 1,2-propanediol. The first method was developed by Brown et al. and the other by Li et al., that differ in their experimental conditions, particularly in glucose concentration (3.57 M in Brown's method versus 0.66 M in Li's).

The synthesized particles were characterized using DLS, Zeta potential, and TEM analyses, which revealed notable differences in their physicochemical properties. Nanoparticles from Brown's method exhibited a larger hydrodynamic diameter (140.70 ± 14.77 nm) with lower polydispersity (PDI: 0.15 ± 0.037), whereas those from Li's protocol were smaller (106.35 ± 2.75 nm) but slightly more polydisperse (PDI: 0.19 ± 0.01). TEM imaging further showed that particles obtained with Li's method had a larger bismuth core (65.63 ± 9.64 nm) compared to those synthesized via Brown's approach (47.3 ± 14.26 nm), which appeared less uniform in shape. These differences suggest that Li's method leads to particles with higher bismuth content and a thinner glucose coating.

UV-Vis spectroscopy confirmed characteristic absorption peaks between 380–400 nm for Brown's particles and 350–400 nm for those from Li's method, while Zeta potential measurements showed a negative surface charge for both formulations, with no significant differences. Long-term stability tests, performed through DLS, Zeta Potential and UV-Vis, confirmed excellent colloidal stability in aqueous suspension for both formulations, attributed to the stabilizing effect of the glucose coating. Further X-ray attenuation studies at varying concentrations demonstrated that both nanoparticle formulations outperformed traditional ICAs, offering improved radiodensity. Moreover, TEM analysis confirmed the superior morphological uniformity and narrower core-size distribution of particles synthesized with Li's method, making them the preferred choice for subsequent surface functionalization steps.

The functionalization was employed through a LbL approach using PAH and PAA as polyelectrolytes and heterobifunctional PEG (NH_2-PEG-COOH) for final PEGylation. Its amine group allowed covalent attachment to the nanoparticle surface via EDC chemistry, while the carboxyl end remained available for subsequent antibody conjugation. Each coating step was monitored by DLS and Zeta potential measurements, which confirmed the successful deposition of each layer through gradual increases in hydrodynamic diameter and alternating zeta potential values. After PEG attachment, the hydrodynamic diameter increased by approximately 45 nm, while the surface charge stayed negative. Further confirmation of PEG deposition layer came from FT-IR spectroscopy, which showed characteristic peaks around 1100 cm^{-1} (C–O–C) and 1700 cm^{-1} (C=O), consistent with the structure of bifunctional PEG. Finally, the stability of the PEGylated formulation was confirmed by the maintenance of hydrodynamic diameter and surface charge over time remaining stable in aqueous suspension within four weeks.

In summary, Bi Nps were successfully developed and functionalized, showing improved physicochemical properties and good surface stability. Thanks to their strong X-ray attenuation and the ability to be functionalized with targeting molecules, these nanoparticles represent a promising platform for contrast-enhanced imaging applications. Future studies could investigate their potential for visualizing specific molecular markers, such as Contactin-2, which is expressed by cells of CCS. This approach may be further developed to assess and validate selective binding to Cntn2, starting with in vitro experiments and progressing to in vivo models, paving the way for future applications in targeted imaging of the CCS.

References

(1) van Weerd, J. H.; Christoffels, V. M. The Formation and Function of the Cardiac Conduction System. *Development* **2016**, *143* (2), 197–210. https://doi.org/10.1242/dev.124883.

(2) Arshad, A.; Atkinson, A. J. A 21st Century View of the Anatomy of the Cardiac Conduction System. *Transl. Res. Anat.* **2022**, *28*, 100204. https://doi.org/10.1016/j.tria.2022.100204.

(3) *What Is the Cardiac Conduction System?*. Cleveland Clinic. https://my.clevelandclinic.org/health/body/21648-heart-conduction-system (accessed 2025-07-13).

(4) Kingma, J.; Simard, C.; Drolet, B. Overview of Cardiac Arrhythmias and Treatment Strategies. *Pharmaceuticals* **2023**, *16* (6), 844. https://doi.org/10.3390/ph16060844.

(5) *How Does Cardiac Ablation Work?*. Cleveland Clinic. https://my.clevelandclinic.org/health/treatments/16851-catheter-ablation (accessed 2025-07-13).

(6) Hosseini, S. M.; Rozen, G.; Saleh, A.; Vaid, J.; Biton, Y.; Moazzami, K.; Heist, E. K.; Mansour, M. C.; Kaadan, M. I.; Vangel, M.; Ruskin, J. N. Catheter Ablation for Cardiac Arrhythmias. *JACC Clin. Electrophysiol.* **2017**, *3* (11), 1240–1248. https://doi.org/10.1016/j.jacep.2017.05.005.

(7) Walsh, K.; Marchlinski, F. Catheter Ablation for Atrial Fibrillation: Current Patient Selection and Outcomes. *Expert Rev. Cardiovasc. Ther.* **2018**, *16* (9), 679–692. https://doi.org/10.1080/14779072.2018.1510317.

(8) Tung, R.; Vaseghi, M.; Frankel, D. S.; Vergara, P.; Di Biase, L.; Nagashima, K.; Yu, R.; Vangala, S.; Tseng, C.-H.; Choi, E.-K.; Khurshid, S.; Patel, M.; Mathuria, N.; Nakahara, S.; Tzou, W. S.; Sauer, W. H.; Vakil, K.; Tedrow, U.; Burkhardt, J. D.; Tholakanahalli, V. N.; Saliaris, A.; Dickfeld, T.; Weiss, J. P.; Bunch, T. J.; Reddy, M.; Kanmanthareddy, A.; Callans, D. J.; Lakkireddy, D.; Natale, A.; Marchlinski, F.; Stevenson, W. G.; Della Bella, P.; Shivkumar, K. Freedom from Recurrent Ventricular Tachycardia after Catheter Ablation Is Associated with Improved Survival in Patients with Structural Heart Disease: An International VT Ablation Center Collaborative Group Study. *Heart Rhythm* **2015**, *12* (9), 1997–2007. https://doi.org/10.1016/j.hrthm.2015.05.036.

(9) Peruzza, F.; Candelora, A.; Angheben, C.; Maines, M.; Laurente, M.; Catanzariti, D.; Del Greco, M.; Madaffari, A. Catheter Ablation of Atrial Fibrillation: Technique and Future Perspectives. *J. Clin. Med.* **2025**, *14* (6), 1788. https://doi.org/10.3390/jcm14061788.

(10) Ma, C.; Chen, T.; Chen, Y.; Ge, J.; Han, W.; Wang, Q.; Zhong, J. Understanding the Scope of Intracardiac Echocardiography in Catheter Ablation of Ventricular Arrhythmia. *Front. Cardiovasc. Med.* **2022**, *9*, 1037176. https://doi.org/10.3389/fcvm.2022.1037176.

(11) Bhakta, D.; Miller, J. M. Principles of Electroanatomic Mapping. *Indian Pacing Electrophysiol. J.* **2008**, *8* (1), 32–50.

(12) Tseng, W.-Y. I.; Su, M.-Y. M.; Tseng, Y.-H. E. Introduction to Cardiovascular Magnetic Resonance: Technical Principles and Clinical Applications. *Acta Cardiol. Sin.* **2016**, *32* (2), 129–144. https://doi.org/10.6515/acs20150616a.

(13) Pontone, G.; Rossi, A.; Guglielmo, M.; Dweck, M. R.; Gaemperli, O.; Nieman, K.; Pugliese, F.; Maurovich-Horvat, P.; Gimelli, A.; Cosyns, B.; Achenbach, S. Clinical Applications of Cardiac Computed Tomography: A Consensus Paper of the European Association of Cardiovascular Imaging-Part I. *Eur. Heart J. Cardiovasc. Imaging* **2022**, *23* (3), 299–314. https://doi.org/10.1093/ehjci/jeab293.

(14) Goldman, L. W. Principles of CT and CT Technology. *J. Nucl. Med. Technol.* **2007**, *35* (3), 115–128. https://doi.org/10.2967/jnmt.107.042978.

(15) Lusic, H.; Grinstaff, M. W. X-Ray-Computed Tomography Contrast Agents. *Chem. Rev.* **2013**, *113* (3), 1641–1666. https://doi.org/10.1021/cr200358s.

(16) Brown, A. Bismuth Nanoparticles as Medical X-Ray Contrast Agents: Synthesis, Characterization and Applications. *Diss. Theses* **2013**. https://doi.org/10.15760/etd.1522.

(17) Hsu, J. C.; Nieves, L. M.; Betzer, O.; Sadan, T.; Noël, P. B.; Popovtzer, R.; Cormode, D. P. Nanoparticle Contrast Agents for X-Ray Imaging Applications. *Wiley Interdiscip. Rev. Nanomed. Nanobiotechnol.* **2020**, *12* (6), e1642. https://doi.org/10.1002/wnan.1642.

(18) Yu, H.; Guo, H.; Wang, Y.; Wang, Y.; Zhang, L. Bismuth Nanomaterials as Contrast Agents for Radiography and Computed Tomography Imaging and Their Quality/Safety Considerations. *WIREs Nanomedicine Nanobiotechnology* **2022**, *14* (6), e1801. https://doi.org/10.1002/wnan.1801.

(19) Douek, P. C.; Boccalini, S.; Oei, E. H. G.; Cormode, D. P.; Pourmorteza, A.; Boussel, L.; Si-Mohamed, S. A.; Budde, R. P. J. Clinical Applications of Photon-Counting CT: A Review of Pioneer Studies and a Glimpse into the Future. *Radiology* **2023**, *309* (1), e222432. https://doi.org/10.1148/radiol.222432.

(20) Liguori, C.; Frauenfelder, G.; Massaroni, C.; Saccomandi, P.; Giurazza, F.; Pitocco, F.; Marano, R.; Schena, E. Emerging Clinical Applications of Computed Tomography. *Med. Devices Auckl. NZ* **2015**, *8*, 265–278. https://doi.org/10.2147/MDER.S70630.

(21) Meulepas, J. M.; Ronckers, C. M.; Smets, A. M. J. B.; Nievelstein, R. A. J.; Gradowska, P.; Lee, C.; Jahnen, A.; van Straten, M.; de Wit, M.-C. Y.; Zonnenberg, B.; Klein, W. M.; Merks, J. H.; Visser, O.; van Leeuwen, F. E.; Hauptmann, M. Radiation Exposure From Pediatric CT Scans and Subsequent Cancer Risk in the Netherlands. *JNCI J. Natl. Cancer Inst.* **2018**, *111* (3), 256–263. https://doi.org/10.1093/jnci/djy104.

(22) Sodickson, A.; Baeyens, P. F.; Andriole, K. P.; Prevedello, L. M.; Nawfel, R. D.; Hanson, R.; Khorasani, R. Recurrent CT, Cumulative Radiation Exposure, and Associated Radiation-Induced Cancer Risks from CT of Adults. *Radiology* **2009**, *251* (1), 175–184. https://doi.org/10.1148/radiol.2511081296.

(23) Burghardt, A. J.; Link, T. M.; Majumdar, S. High-Resolution Computed Tomography for Clinical Imaging of Bone Microarchitecture. *Clin. Orthop.* **2011**, *469* (8), 2179–2193. https://doi.org/10.1007/s11999-010-1766-x.

(24) Caschera, L.; Lazzara, A.; Piergallini, L.; Ricci, D.; Tuscano, B.; Vanzulli, A. Contrast Agents in Diagnostic Imaging: Present and Future. *Pharmacol. Res.* **2016**, *110*, 65–75. https://doi.org/10.1016/j.phrs.2016.04.023.

(25) Kaller, M. O.; An, J. Contrast Agent Toxicity. In *StatPearls*; StatPearls Publishing: Treasure Island (FL), 2024.

(26) Davenport, M. S.; Perazella, M. A.; Yee, J.; Dillman, J. R.; Fine, D.; McDonald, R. J.; Rodby, R. A.; Wang, C. L.; Weinreb, J. C. Use of Intravenous Iodinated Contrast Media in Patients with Kidney Disease: Consensus Statements from the American College of Radiology and the National Kidney Foundation. *Radiology* **2020**, *294* (3), 660–668. https://doi.org/10.1148/radiol.2019192094.

(27) Pasternak, J. J.; Williamson, E. E. Clinical Pharmacology, Uses, and Adverse Reactions of Iodinated Contrast Agents: A Primer for the Non-Radiologist. *Mayo Clin. Proc.* **2012**, *87* (4), 390–402. https://doi.org/10.1016/j.mayocp.2012.01.012.

(28) Cai, Q.-Y.; Kim, S. H.; Choi, K. S.; Kim, S. Y.; Byun, S. J.; Kim, K. W.; Park, S. H.; Juhng, S. K.; Yoon, K.-H. Colloidal Gold Nanoparticles as a Blood-Pool Contrast Agent for X-Ray Computed Tomography in Mice. *Invest. Radiol.* **2007**, *42* (12), 797–806. https://doi.org/10.1097/RLI.0b013e31811ecdcd.

(29) Piechowiak, E. I.; Peter, J.-F. W.; Kleb, B.; Klose, K. J.; Heverhagen, J. T. Intravenous Iodinated Contrast Agents Amplify DNA Radiation Damage at CT. *Radiology* **2015**, *275* (3), 692–697. https://doi.org/10.1148/radiol.14132478.

(30) Fernandez-Antoran, D.; Piedrafita, G.; Murai, K.; Ong, S. H.; Herms, A.; Frezza, C.; Jones, P. H. Outcompeting P53-Mutant Cells in the Normal Esophagus by Redox Manipulation. *Cell Stem Cell* **2019**, *25* (3), 329-341.e6. https://doi.org/10.1016/j.stem.2019.06.011.

(31) Menon, M. C.; Chuang, P. Y.; He, C. J. The Glomerular Filtration Barrier: Components and Crosstalk. *Int. J. Nephrol.* **2012**, *2012* (1), 749010. https://doi.org/10.1155/2012/749010.

(32) Scott, R. P.; Quaggin, S. E. The Cell Biology of Renal Filtration. *J. Cell Biol.* **2015**, *209* (2), 199–210. https://doi.org/10.1083/jcb.201410017.

(33) Longmire, M.; Choyke, P. L.; Kobayashi, H. Clearance Properties of Nano-Sized Particles and Molecules as Imaging Agents: Considerations and Caveats. *Nanomed.* **2008**, *3* (5), 703–717. https://doi.org/10.2217/17435889.3.5.703.

(34) Lee, N.; Choi, S. H.; Hyeon, T. Nano-Sized CT Contrast Agents. *Adv. Mater. Deerfield Beach Fla* **2013**, *25* (19), 2641–2660. https://doi.org/10.1002/adma.201300081.

(35) De La Vega, J. C.; Häfeli, U. O. Utilization of Nanoparticles as X-Ray Contrast Agents for Diagnostic Imaging Applications. *Contrast Media Mol. Imaging* **2015**, *10* (2), 81–95. https://doi.org/10.1002/cmmi.1613.

(36) Xiong, P.; Huang, X.; Ye, N.; Lu, Q.; Zhang, G.; Peng, S.; Wang, H.; Liu, Y. Cytotoxicity of Metal-Based Nanoparticles: From Mechanisms and Methods of Evaluation to Pathological Manifestations. *Adv. Sci.* **2022**, *9* (16), 2106049. https://doi.org/10.1002/advs.202106049.

(37) FitzGerald, P. F.; Butts, M. D.; Roberts, J. C.; Colborn, R. E.; Torres, A. S.; Lee, B. D.; Yeh, B. M.; Bonitatibus, P. J. J. A Proposed Computed Tomography Contrast Agent Using Carboxybetaine Zwitterionic Tantalum Oxide Nanoparticles: Imaging, Biological, and Physicochemical Performance. *Invest. Radiol.* **2016**, *51* (12), 786. https://doi.org/10.1097/RLI.0000000000000279.

(38) Zhou, C.; Long, M.; Qin, Y.; Sun, X.; Zheng, J. Luminescent Gold Nanoparticles with Efficient Renal Clearance. *Angew. Chem. Int. Ed Engl.* **2011**, *50* (14), 3168–3172. https://doi.org/10.1002/anie.201007321.

(39) Ahmad, M. Y.; Liu, S.; Tegafaw, T.; Saidi, A. K. A. A.; Zhao, D.; Liu, Y.; Nam, S.-W.; Chang, Y.; Lee, G. H. Heavy Metal-Based Nanoparticles as High-Performance X-Ray Computed Tomography Contrast Agents. *Pharmaceuticals* **2023**, *16* (10), 1463. https://doi.org/10.3390/ph16101463.

(40) Ahn, S.; Jung, S. Y.; Lee, S. J. Gold Nanoparticle Contrast Agents in Advanced X-Ray Imaging Technologies. *Mol. Basel Switz.* **2013**, *18* (5), 5858–5890. https://doi.org/10.3390/molecules18055858.

(41) Kim, D.; Park, S.; Lee, J. H.; Jeong, Y. Y.; Jon, S. Antibiofouling Polymer-Coated Gold Nanoparticles as a Contrast Agent for in Vivo X-Ray Computed Tomography Imaging. *J. Am. Chem. Soc.* **2007**, *129* (24), 7661–7665. https://doi.org/10.1021/ja071471p.

(42) Khlebtsov, N.; Dykman, L. Biodistribution and Toxicity of Engineered Gold Nanoparticles: A Review of in Vitro and in Vivo Studies. *Chem. Soc. Rev.* **2011**, *40* (3), 1647–1671. https://doi.org/10.1039/c0cs00018c.

(43) Liu, Y.; Ai, K.; Lu, L. Nanoparticulate X-Ray Computed Tomography Contrast Agents: From Design Validation to in Vivo Applications. *Acc. Chem. Res.* **2012**, *45* (10), 1817–1827. https://doi.org/10.1021/ar300150c.

(44) Mohan, R. Green Bismuth. *Nat. Chem.* **2010**, *2* (4), 336–336. https://doi.org/10.1038/nchem.609.

(45) Gilster, J.; Bacon, K.; Marlink, K.; Sheppard, B.; Deveney, C.; Rutten, M. Bismuth Subsalicylate Increases Intracellular Ca2+, MAP-Kinase Activity, and Cell Proliferation in Normal Human Gastric Mucous Epithelial Cells. *Dig. Dis. Sci.* **2004**, *49* (3), 370–378. https://doi.org/10.1023/b:ddas.0000020488.55854.99.

(46) Luo, Y.; Wang, C.; Qiao, Y.; Hossain, M.; Ma, L.; Su, M. In Vitro Cytotoxicity of Surface Modified Bismuth Nanoparticles. *J. Mater. Sci. Mater. Med.* **2012**, *23* (10), 2563–2573. https://doi.org/10.1007/s10856-012-4716-1.

(47) Brown, A. L.; Naha, P. C.; Benavides-Montes, V.; Litt, H. I.; Goforth, A. M.; Cormode, D. P. Synthesis, X-Ray Opacity, and Biological Compatibility of Ultra-High Payload Elemental Bismuth Nanoparticle X-Ray Contrast Agents. *Chem. Mater. Publ. Am. Chem. Soc.* **2014**, *26* (7), 2266–2274. https://doi.org/10.1021/cm500077z.

(48) Li, Z.; Liu, J.; Hu, Y.; Li, Z.; Fan, X.; Sun, Y.; Besenbacher, F.; Chen, C.; Yu, M. Biocompatible PEGylated Bismuth Nanocrystals: "All-in-One" Theranostic Agent with Triple-Modal Imaging and Efficient in Vivo Photothermal Ablation of Tumors. *Biomaterials* **2017**, *141*, 284–295. https://doi.org/10.1016/j.biomaterials.2017.06.033.

(49) Li, Z.; Fan, X.; Liu, J.; Hu, Y.; Yang, Y.; Li, Z.; Sun, Y.; Chen, C.; Yu, M. Mesoporous Silica-Coated Bismuth Nanohybrids as a New Platform for Photoacoustic/Computed Tomography Imaging and Synergistic Chemophotothermal Therapy. *Nanomed.* **2018**, *13* (18), 2283–2300. https://doi.org/10.2217/nnm-2018-0106.

(50) Wei, B.; Zhang, X.; Zhang, C.; Jiang, Y.; Fu, Y.-Y.; Yu, C.; Sun, S.-K.; Yan, X.-P. Facile Synthesis of Uniform-Sized Bismuth Nanoparticles for CT Visualization of Gastrointestinal Tract in Vivo. *ACS Appl. Mater. Interfaces* **2016**, *8* (20), 12720–12726. https://doi.org/10.1021/acsami.6b03640.

(51) Mjos, K. D.; Orvig, C. Metallodrugs in Medicinal Inorganic Chemistry. *Chem. Rev.* **2014**, *114* (8), 4540–4563. https://doi.org/10.1021/cr400460s.

(52) Swy, E. R.; Schwartz-Duval, A. S.; Shuboni, D. D.; Latourette, M. T.; Mallet, C. L.; Parys, M.; Cormode, D. P.; Shapiro, E. M. Dual-Modality, Fluorescent, PLGA Encapsulated Bismuth Nanoparticles for Molecular and Cellular Fluorescence Imaging and Computed Tomography. *Nanoscale* **2014**, *6* (21), 13104–13112. https://doi.org/10.1039/C4NR01405G.

(53) Chen, J.; Yang, X.-Q.; Meng, Y.-Z.; Huang, H.-H.; Qin, M.-Y.; Yan, D.-M.; Zhao, Y.-D.; Ma, Z.-Y. In Vitro and in Vivo CT Imaging Using Bismuth Sulfide Modified with a Highly Biocompatible Pluronic F127. *Nanotechnology* **2014**, *25* (29), 295103. https://doi.org/10.1088/0957-4484/25/29/295103.

(54) Bi, H.; He, F.; Dong, Y.; Yang, D.; Dai, Y.; Xu, L.; Lv, R.; Gai, S.; Yang, P.; Lin, J. Bismuth Nanoparticles with "Light" Property Served as a Multifunctional Probe for X-Ray Computed Tomography and Fluorescence Imaging. *Chem. Mater.* **2018**, *30* (10), 3301–3307. https://doi.org/10.1021/acs.chemmater.8b00565.

(55) Yu, X.; Li, A.; Zhao, C.; Yang, K.; Chen, X.; Li, W. Ultrasmall Semimetal Nanoparticles of Bismuth for Dual-Modal Computed Tomography/Photoacoustic Imaging and Synergistic Thermoradiotherapy. *ACS Nano* **2017**, *11* (4), 3990–4001. https://doi.org/10.1021/acsnano.7b00476.

(56) Lei, P.; An, R.; Zheng, X.; Zhang, P.; Du, K.; Zhang, M.; Dong, L.; Gao, X.; Feng, J.; Zhang, H. Ultrafast Synthesis of Ultrasmall Polyethylenimine-Protected AgBiS2 Nanodots by "Rookie Method" for in Vivo Dual-

Modal CT/PA Imaging and Simultaneous Photothermal Therapy. *Nanoscale* **2018**, *10* (35), 16765–16774. https://doi.org/10.1039/c8nr04870c.

(57) Yu, N.; Wang, Z.; Zhang, J.; Liu, Z.; Zhu, B.; Yu, J.; Zhu, M.; Peng, C.; Chen, Z. Thiol-Capped Bi Nanoparticles as Stable and All-in-One Type Theranostic Nanoagents for Tumor Imaging and Thermoradiotherapy. *Biomaterials* **2018**, *161*, 279–291. https://doi.org/10.1016/j.biomaterials.2018.01.047.

(58) Pan, D.; Roessl, E.; Schlomka, J.-P.; Caruthers, S. D.; Senpan, A.; Scott, M. J.; Allen, J. S.; Zhang, H.; Hu, G.; Gaffney, P. J.; Choi, E. T.; Rasche, V.; Wickline, S. A.; Proksa, R.; Lanza, G. M. Computed Tomography in Color: NanoK-Enhanced Spectral CT Molecular Imaging. *Angew. Chem. Int. Ed Engl.* **2010**, *49* (50), 9635–9639. https://doi.org/10.1002/anie.201005657.

(59) Pallante, B. A.; Giovannone, S.; Fang-Yu, L.; Zhang, J.; Liu, N.; Kang, G.; Dun, W.; Boyden, P. A.; Fishman, G. I. Contactin-2 Expression in the Cardiac Purkinje Fiber Network. *Circ. Arrhythm. Electrophysiol.* **2010**, *3* (2), 186–194. https://doi.org/10.1161/CIRCEP.109.928820.

(60) (PDF) Particle Size Distribution and Zeta Potential Based on Dynamic Light Scattering: Techniques to Characterise Stability and Surface Distribution of Charged Colloids. In *ResearchGate*.

(61) *Zetasizer Pro - Zeta Potential Analysis System*. https://www.malvernpanalytical.com/en/products/product-range/zetasizer-range/zetasizer-advance-range/zetasizer-pro (accessed 2025-07-14).

(62) Gomez, C.; Hallot, G.; Pastor, A.; Laurent, S.; Brun, E.; Sicard-Roselli, C.; Port, M. Metallic Bismuth Nanoparticles: Towards a Robust, Productive and Ultrasound Assisted Synthesis from Batch to Flow-Continuous Chemistry. *Ultrason. Sonochem.* **2019**, *56*, 167–173. https://doi.org/10.1016/j.ultsonch.2019.04.012.

(63) Titus, D.; James Jebaseelan Samuel, E.; Roopan, S. M. Chapter 12 - Nanoparticle Characterization Techniques. In *Green Synthesis, Characterization and Applications of Nanoparticles*; Shukla, A. K., Iravani, S., Eds.; Micro and Nano Technologies; Elsevier, 2019; pp 303–319. https://doi.org/10.1016/B978-0-08-102579-6.00012-5.

(64) *Versatile, Routine UV-Vis Instrument, Cary 60 | Agilent*. https://www.agilent.com/en/product/molecular-spectroscopy/uv-vis-uv-vis-nir-spectroscopy/uv-vis-uv-vis-nir-systems/cary-60-uv-vis-spectrophotometer?gclsrc=aw.ds&gad_source=1&gad_campaignid=21858641697&gclid=CjwKCAjw1dLDBhBoEiwAQNRiQf3fXkTgdvIQhf0jTQTHi1HEaQQCDGLVVXQ0e8btTt7efGYIvVXs6xoCL-QQAvD_BwE (accessed 2025-07-14).

(65) *Optical Emission Spectrometer, OES spectrometer, 5800 ICP-OES | Agilent*. https://www.agilent.com/en/product/atomic-spectroscopy/inductively-coupled-plasma-optical-emission-spectroscopy-icp-oes/icp-oes-instruments/5800-icp-oes?gclsrc=aw.ds&gad_source=1&gad_campaignid=21858641697&gclid=CjwKCAjw1dLDBhBoEiwAQNRiQU6ecj88vDAwG0XpT7s3NvEnsb_-qFSlURofi2Wr1WHD1AOGsF7OzBoC6ygQAvD_BwE (accessed 2025-07-14).

(66) Dos Anjos, S. L.; Alves, J. C.; Rocha Soares, S. A.; Araujo, R. G. O.; de Oliveira, O. M. C.; Queiroz, A. F. S.; Ferreira, S. L. C. Multivariate Optimization of a Procedure Employing Microwave-Assisted Digestion for the Determination of Nickel and Vanadium in Crude Oil by ICP OES. *Talanta* **2018**, *178*, 842–846. https://doi.org/10.1016/j.talanta.2017.10.010.

(67) *FEI G2 F20 TEM 200kV – UF ICBR*. https://biotech.ufl.edu/portfolio/fei-g2-f20-tem-200kv-2/ (accessed 2025-07-14).

(68) *Nicolet 6700 FT-IR Spectrometer from Thermo Fisher Scientific - Product Description and Details*. https://www.americanpharmaceuticalreview.com/25304-Pharmaceutical-Infrared-Spectroscopy-Equipment-Infrared-Spectrometers/5822268-Nicolet-6700-FT-IR-Spectrometer/ (accessed 2025-07-14).

(69) *In Vivo MicroCT | High Resolution | Desktop*. https://www.bruker.com/it/products-and-solutions/preclinical-imaging/micro-ct/skyscan-1276.html (accessed 2025-07-14).

(70) Schneider, G.; Decher, G. Functional Core/Shell Nanoparticles via Layer-by-Layer Assembly. Investigation of the Experimental Parameters for Controlling Particle Aggregation and for Enhancing Dispersion Stability. *Langmuir ACS J. Surf. Colloids* **2008**, *24* (5), 1778–1789. https://doi.org/10.1021/la7021837.